PACS photometer point spread function

Dieter Lutz

Contents

1 Summary

The PACS Performance Verification (PV) and routine calibration plan includes a broad range of observations aiming to characterise the PSF for a wide range of observing modes and source SEDs. The distinction between different SEDs is made because of the expected dependence of PSF width on SED slope, which is due to the wide PACS filter bandpasses.

Version 2.2 of this note presents results derived from scanmap observations during various PV and routine phase calibrations using the star α Tau and the asteroids Vesta and Ceres. These are all 'hot' sources for PACS, with different flux levels. α Tau is within the unsaturated and linear flux range. Ceres and to a lesser extent Vesta enter the regime where nonlinearity effects start to be noticeable in the brightest regions of the PSF core, first in the blue band. Mars, Neptune, IK Tau and the Red Rectangle are used as extremely bright targets for characterizing PSF wings and to probe for ghosts and straylight. This is done realizing they are not point sources and may be saturated or significantly into the nonlinear regime in parts of the PSF cores.

A final PSF characterisation may use a yet wider set of observations and make use of calibrations and reduction steps that are currently not yet available. PSF images for Vesta are released along with this note. *We emphasize that the true PSF of a given science observation may differ in detail from what is presented here.* Such variations may occur for the PSF core due to pointing jitter during the scans and *in particular due to specific data reduction steps taken.* Variations from observation to observation are also possible for the faintest PSF wings, since some of the crosstalk/straylight/ghost effects discussed below depend on the exact path that the source has taken across the PACS arrays.

The photometer PSF is characterised by:

- A narrow core which is round in the blue and green bands but slightly elongated in spacecraft Z direction[1] in red.
- A tri-lobe pattern seen at the several % level in all bands, most clearly in the blue with its strongest signal. It is ascribed to imperfect shape of the Herschel primary mirror.
- Knotty structured diffraction 'rings' at sub-percent level, clearly seen in blue and green.

For fast scans in normal and in parallel mode, this PSF structure is smeared in scan direction by detector time constants and by the on-board data averaging.

The most prominent unusual effects are: (1) A narrow and faint spike, extending in Z direction. This spike is seen in blue and green and also indicated in red. (2) A negative PSF feature in the scan direction of blue/green fast scans which is indicative of an undershooting of the signal after source passage. (3) Negative ghost images due to detector crosstalk. (4) Several types of weak ghost reflections occuring, for example, when the source is just off the array corners.

At the faint levels of the PSF the six-spoke diffraction pattern is seen. This pattern is caused by the secondary mirror support.

[1]For the orientation of the spacecraft Y,Z directions on sky with respect to the PACS arrays see, e.g., Fig. 15 or document PICC-ME-TN-027

A set of PACS modelled PSFs is independently presented in document PICC-ME-TN-029, which in its version 2.0 is including an 'as built' telescope model that is implementing pre-launch knowledge on the telescope wavefront errors. While these modelled PSFs reproduce many salient features of the observed PSF, they are not realistic enough for use in tasks that require accurate PSFs, like PSF fitting and deconvolution. By definition they refer to the Herschel telescope only and will not include ghosts etc. that are arising in PACS.

2 Data reference sheet

See Table 1.

3 Description of observations

The original dedicated PSF observations are scanmaps centered on the star α Tau (OD118), the asteroid Vesta (OD160), and the blazar 3C345 (OD124), using 15 scanlegs with 3 arcsec cross-scan separation. The array-to-map angle specifying the scan direction is 63 degree in the instrument reference frame, roughly along the array diagonal[2]. This pattern is overall providing source passages over many regions of the array and with good sub-pixel sampling. For Vesta, additional observations were taken in medium and fast scan and at the SPIRE/PACS parallel mode 'magic' array-to-map angle $\pm$42 degrees (OD345). Results from these Vesta observations were validated using OD269 true parallel mode observations of αBoo.

Scanmaps of Mars (OD137, OD888) Neptune (OD173) and Ceres (OD734, OD782) are used to investigate fainter PSF structures.

The Mars observations, in particular the specially designed ones from OD906, are also useful to map out reflections and other artefacts that are found when a very bright source is on or near the array.

Fluxes of the sources used in this note are listed in Table 3. For variable and solar system sources, the appropriate OD is also noted.

4 Analysis methods and reduction scripts used

We create two basic versions of the PSFs: One is created from a rather normal PACS highpass-filtered scanmap reduction. For the best fidelity PSF results we also obtain 'recentered' PSFs by a posteriori correcting for pointing variations. Here we use two main reduction steps (1) determination of pointing corrections and (2) mapping. In the cases with normal processing, step (1) is skipped.

Pointing corrections for the 'recentering' are determined in the first pass by comparing frame per frame the

[2]We use the 'array-to-map angle' in the sense of section 5.1 of the PACS Observer's manual, denoted α in Figure 5.2 of that manual, see also the Appendix to this note

OD	OBSID	Source	HSPOT name	Time sec	ama deg
118	1342183538	αTau	Calibration_PVPhotSpatial_1-PVPhotSpatial_314D_StdScan_blumed_AlfTau_0001	853	63
118	1342183539	αTau	Calibration_PVPhotSpatial_1-PVPhotSpatial_314D_StdScan_bluhigh_AlfTau_0001	819	63
118	1342183540	αTau	Calibration_PVPhotSpatial_1-PVPhotSpatial_314D_StdScan_blulow_AlfTau_0001	1215	63
118	1342183541	αTau	Calibration_PVPhotSpatial_1-PVPhotSpatial_314D_StdScan_grnmed_AlfTau_0001	853	63
118	1342183542	αTau	Calibration_PVPhotSpatial_1-PVPhotSpatial_314D_StdScan_grnhigh_AlfTau_0001	819	63
118	1342183543	αTau	Calibration_PVPhotSpatial_1-PVPhotSpatial_314D_StdScan_grnlow_AlfTau_0001	1215	63
119	1342183556	Red Rect	Calibration_PVPhotSpatial_1-PVPhotSpatial_315B_StdScan_blu_RedRect_0001	13245	63
119	1342183559	IK Tau	Calibration_PVPhotSpatial_1-PVPhotSpatial_316A_StdScan_blu_IKTau_0001	6481	20
124	1342183880	3C345	Calibration_PVPhotSpatial_1-PVPhotSpatial_314D_StdScan_bluhigh_3C345_0001	819	63
124	1342183881	3C345	Calibration_PVPhotSpatial_1-PVPhotSpatial_314D_StdScan_blumed_3C345_0001	853	63
124	1342183882	3C345	Calibration_PVPhotSpatial_1-PVPhotSpatial_314D_StdScan_blulow_3C345_0001	1215	63
124	1342183883	3C345	Calibration_PVPhotSpatial_1-PVPhotSpatial_314D_StdScan_grnlow_3C345_0001	1215	63
124	1342183884	3C345	Calibration_PVPhotSpatial_1-PVPhotSpatial_314D_StdScan_grnmed_3C345_0001	853	63
124	1342183885	3C345	Calibration_PVPhotSpatial_1-PVPhotSpatial_314D_StdScan_grnhigh_3C345_0001	819	63
137	1342184486	Mars	Calibration_PVParStray_1-PVParStray_316A_TFOV_blu2dx2d_centre_Mars_OD137	11044	Nom
137	1342184487	Mars	Calibration_PVParStray_1-PVParStray_316A_TFOV_blu2x2d_centre_Mars_off1_OD137	11044	Nom
137	1342184488	Mars	Calibration_PVParStray_1-PVParStray_316A_TFOV_blu2x2d_centre_Mars_off2_OD137	11044	Nom
160	1342186132	Vesta	Calibration_PVPhotSpatial_1-PVPhotSpatial_314D_StdScan_grnlow_Vesta_0001	1407	63
160	1342186133	Vesta	Calibration_PVPhotSpatial_1-PVPhotSpatial_314D_StdScan_grnmed_Vesta_0001	1045	63
160	1342186134	Vesta	Calibration_PVPhotSpatial_1-PVPhotSpatial_314D_StdScan_grnhigh_Vesta_0001	1011	63
160	1342186135	Vesta	Calibration_PVPhotSpatial_1-PVPhotSpatial_314D_StdScan_blulow_Vesta_0001	1407	63
160	1342186136	Vesta	Calibration_PVPhotSpatial_1-PVPhotSpatial_314D_StdScan_blumed_Vesta_0001	1045	63
160	1342186137	Vesta	Calibration_PVPhotSpatial_1-PVPhotSpatial_314D_StdScan_bluhigh_Vesta_0001	1011	63
173	1342186639	Neptune	Calibration_PVPhotFlux_1-PVPhotFlux_321D_StdScan_045_pcal_blu_Neptune_0001	179	45
173	1342186640	Neptune	Calibration_PVPhotFlux_1-PVPhotFlux_321D_StdScan_135_pcal_blu_Neptune_0001	179	135
173	1342186641	Neptune	Calibration_PVPhotFlux_1-PVPhotFlux_321D_StdScan_045_pcal_grn_Neptune_0001	179	45
173	1342186642	Neptune	Calibration_PVPhotFlux_1-PVPhotFlux_321D_StdScan_135_pcal_grn_Neptune_0001	179	135
269	1342190261	αBoo	Calibration_RPParAOTVal_515A_StdNom_blu_slow_alfBoo_0001	3760	42
269	1342190262	αBoo	Calibration_RPParAOTVal_515A_StdOrt_blu_slow_alfBoo_0001	3760	-42
269	1342190263	αBoo	Calibration_RPParAOTVal_515A_StdNom_blu_fast_alfBoo_0001	1909	42
269	1342190264	αBoo	Calibration_RPParAOTVal_515A_StdOrt_blu_fast_alfBoo_0001	1909	-42
269	1342190265	αBoo	Calibration_RPParAOTVal_515A_StdNom_grn_slow_alfBoo_0001	3760	42
269	1342190266	αBoo	Calibration_RPParAOTVal_515A_StdOrt_grn_slow_alfBoo_0001	3760	-42
269	1342190267	αBoo	Calibration_RPParAOTVal_515A_StdNom_grn_fast_alfBoo_0001	1909	42
269	1342190268	αBoo	Calibration_RPParAOTVal_515A_StdOrt_grn_fast_alfBoo_0001	1909	-42
345	1342195470	Vesta	Calibration_RPPhotSpatial_1-RPPhotSpatial_314A_StdScan+42_hi_blu_Vesta_0001	703	42
345	1342195471	Vesta	Calibration_RPPhotSpatial_1-RPPhotSpatial_314A_StdScan-42_hi_blu_Vesta_0001	703	-42
345	1342195472	Vesta	Calibration_RPPhotSpatial_1-RPPhotSpatial_314A_StdScan+42_med_blu_Vesta_0001	741	42
345	1342195473	Vesta	Calibration_RPPhotSpatial_1-RPPhotSpatial_314A_StdScan-42_med_blu_Vesta_0001	741	-42
345	1342195474	Vesta	Calibration_RPPhotSpatial_1-RPPhotSpatial_314A_StdScan+42_hi_grn_Vesta_0001	703	42
345	1342195475	Vesta	Calibration_RPPhotSpatial_1-RPPhotSpatial_314A_StdScan-42_hi_grn_Vesta_0001	703	-42
345	1342195476	Vesta	Calibration_RPPhotSpatial_1-RPPhotSpatial_314A_StdScan+42_med_grn_Vesta_0001	741	42
345	1342195477	Vesta	Calibration_RPPhotSpatial_1-RPPhotSpatial_314A_StdScan-42_med_grn_Vesta_0001	741	-42
348	1342195622	Vesta	Calibration_RPPhotSpatial_1-RPPhotSpatial_314B_StdScan+20_med_grn_Vesta_0001	3926	20
734	1342221350	Ceres	Calibration_RPPhotSpatial_1-RPPhotSpatial_314D_StdScan045_med_blue_Ceres_0001	1055	45
734	1342221351	Ceres	Calibration_RPPhotSpatial_1-RPPhotSpatial_314D_StdScan135_med_blue_Ceres_0001	1055	135
734	1342221352	Ceres	Calibration_RPPhotSpatial_1-RPPhotSpatial_314D_StdScan045_med_grn_Ceres_0001	1055	45
734	1342221353	Ceres	Calibration_RPPhotSpatial_1-RPPhotSpatial_314D_StdScan135_med_grn_Ceres_0001	1055	135
782	1342223701	Ceres	Calibration_RPPhotSpatial_1-RPPhotSpatial_314D_StdScan045_med_blue_Ceres_0002	1055	45
782	1342223702	Ceres	Calibration_RPPhotSpatial_1-RPPhotSpatial_314D_StdScan135_med_blue_Ceres_0002	1055	135
782	1342223706	Ceres	Calibration_RPPhotSpatial_1-RPPhotSpatial_314D_StdScan045_med_grn_Ceres_0002	1055	45
782	1342223707	Ceres	Calibration_RPPhotSpatial_1-RPPhotSpatial_314D_StdScan135_med_grn_Ceres_0002	1055	135
888	1342231157	Mars	Calibration_RPPhotSpatial_1-RPPhotSpatial_314E_StdScan045_hi_blue_Mars_0001	3729	45
888	1342231158	Mars	Calibration_RPPhotSpatial_1-RPPhotSpatial_314E_StdScan135_hi_blue_Mars_0001	3729	135
888	1342231159	Mars	Calibration_RPPhotSpatial_1-RPPhotSpatial_314E_StdScan225_hi_blue_Mars_0001	3729	45
888	1342231160	Mars	Calibration_RPPhotSpatial_1-RPPhotSpatial_314E_StdScan315_hi_blue_Mars_0001	3729	135
888	1342231161	Mars	Calibration_RPPhotSpatial_1-RPPhotSpatial_314E_StdScan045_hi_grn_Mars_0001	3729	45
888	1342231162	Mars	Calibration_RPPhotSpatial_1-RPPhotSpatial_314E_StdScan135_hi_grn_Mars_0001	3729	135
888	1342231163	Mars	Calibration_RPPhotSpatial_1-RPPhotSpatial_314E_StdScan225_hi_grn_Mars_0001	3729	45
888	1342231164	Mars	Calibration_RPPhotSpatial_1-RPPhotSpatial_314E_StdScan315_hi_grn_Mars_0001	3729	135
906	1342231949	Mars	Calibration_RPPhotSpatial_1-RPPhotSpatial_315B_StdScan090_med_blu_Mars_0001	3245	90
906	1342231950	Mars	Calibration_RPPhotSpatial_1-RPPhotSpatial_315B_StdScan090_med_grn_Mars_0001	3245	90

Table 1: Data used for this note. ama denotes the array-to-map angle (scan direction) in degrees CCW from the spacecraft Z direction.

expected location of the source on the array (computed from pointing product information and PACS spatial calibration) with the measured position from a 2-dimensional gaussian fit. Only frames for which the source was centered at least 1.5 pixels inside a detector matrix were kept. The corrections derived were then used in the second pass processing to adjust the input RA, DEC coordinates of each frame to achieve consistency between expected and actual centroid on the frame. Given instantaneous S/N in the respective filters, corrections were derived from the blue/green data and applied also to the red data, considering the time shift of the frame indices

Source	OD	S(70) Jy	S(100) Jy	S(160) Jy	Reference
αTau	any	14.0	6.9	2.7	PACS PV plan PICC-MA-PL-001
3C345	124	0.27	0.40	0.69	PACS data
Ceres	734	187.2	108.4	46.6	T.M. 24.01.2012
Ceres	782	287.0	166.3	71.5	T.M. 24.01.2012
Mars	137	61900	34300	15500	T.M. 13.08.2010
Mars	888	44670	24740	11160	T.M. 21.11.2011
Mars	906	53240	29490	13310	T.M. 21.11.2011
Vesta	160	92.6	48.5	19.8	T.M. 26.10.2009
Vesta	345	199.0	104.0	42.4	T.M. 23.02.2012
Vesta	348	196.0	102.6	41.8	T.M. 23.02.2012
Neptune	173	353	357	260	T.M. 13.08.2010

Table 2: Source fluxes in the PACS bands adopted in this note. The fluxes of solar system objects are private communication by Thomas Müller (dated). Variations at the % level that may happen during the observations of each OD are not traced here. The 3C345 fluxes are quick/approximate from the PACS reduction, serving to indicate the spectral slope.

in each camera. This procedure was applied only to the αTau and Vesta data. By definition, it produces small PSF images reaching away from the source by at most an array size, since the source has to be on the array for derivation of the recentering correction. By definition, it will also suppress those ghosts which are occuring while the source is off the array.

The second pass is a standard highpass-filtered/photProject scanmap production, making use of the corrected pointing (if recentering) or the nominal Herschel pointing otherwise. Build 8.0 3282 and calibration version PACS_CAL_38_0 was used for the v2.0 PSF processing that is described in this version of the document. Points worth being noted are:

- Calblock related steps and drift correction were bypassed. This is now also the pipeline default.
- For the first time in v2.0 of the PSF reduction, we used the photMaskCrosstalk task to eliminate the first columns of all detector matrices, which are affected by crosstalk. This is now common practice for many user reductions of bright sources, where PSF detail counts. We nevertheless kept the discussion of the effects that occur if these columns are still used.
- For the first time in v1.0 we used second level deglitching in the timeordered mode. For Mars with its straylight and saturation effects we relaxed the detection threshold within 5 arcmin and completely suppressed deglitching within 2 arcmin. Still, there are for Mars some remaining effects of deglitching e.g. in regions crossed by a detector that was previously saturated while crossing the planet, and now showing aftereffects of the saturation.
- For the first time in v2.0 we applied the nonlinearity correction that is derived as described in PICC-NHSC-TR-031 and implemented in the photNonLinearityCorrection task.
- To span the commonly used range of 'drizzling' parameters in the photProject map making, we derived and deliver PSFs both for the default pixfrac=1.0 setting and for a small pixfrac=0.1 drop size. An example of finer parameter space sampling including variations of the map pixel size is given in Sect. 7.4.
- Coverage maps were checked and had no dips at the source position any more, except for saturated sources. If not masking crosstalk affected columns, coverage dips are often present in the region affected by crosstalk, separated by one matrix size from the source. Since this crosstalk is seen in only part of the pixels that crossed a given spot on sky, it is identified by the 2nd level deglitching if the source is bright.

Source	OD	dRA/dt deg/h	dDEC/dt deg/h
Mars	137	0.025299	-0.002823
Vesta	160	0.014853	-0.003412
Neptune	173	-0.000036	-0.000015
Vesta	345	0.004937	-0.003147
Vesta	348	0.005746	-0.003431
Ceres	734	0.011501	0.002875
Ceres	782	0.005506	-0.000625
Mars	888	0.023464	-0.006722
Mars	906	0.021165	-0.006889

Table 3: Proper motions adopted for the SSO observations used in this note (based on input provided by T. Müller)

- A region centered on the source with 60 arcsec radius (αTau, most Vesta observations) or larger (for brighter sources and larger maps) was masked in the highpass filtering to suppress the familiar filtering residues on both sides of the bright source. A highpass filter radius of 100 arcsec on sky (for 60arcsec masking radius, larger otherwise) was used.
- All maps were projected on a 1 arcsec pixel grid with a map orientation based on the spacecraft position angle at the time of the observation (see also Appendix). As a consequence, the PSF image axes align with the spacecraft Y,Z directions as if the spacecraft position angle would have been 0. When we refer to 'position angles' of structures below these are 'east of north' (ccw) relative to the spacecraft Z axis which is pointing upwards in the PSF images, rather than relative to the actual north direction of the particular observation. The sources are centered on a single pixel at the map center. We have enforced this pixel centering despite satellite pointing offsets.
- To ensure a clearly defined zero point in flux, all PSFs were explicitly corrected to background 0 in an annular aperture of width 10 arcsec just outside the masking radius use, using the 'Daophot' algorithm=4 of annularSkyAperturePhotometry. Note that this has implications for the encircled energy fraction discussion below.

All the data (except Mars OD137 and αBoo OD269, which were observed in parallel mode) were taken in standard PACS prime scan mode but we partly simulate the blue/green PSF for parallel mode at 60arcsec/sec (fast) and 20arcsec/sec (medium speed). The parallel mode in blue/green is on-board averaging 8 rather than 4 40Hz samples. We simulate this in reduction from standard scans by averaging the fluxes and coordinates of 2 consecutive frames of our data, which were already on-board averaged for 4 samples at 40Hz.

The data for Vesta, a solar system object moving at 53arcsec/h at the time of the OD160 observations, as well as all other SSOs, were made amenable to the same processing by applying a suitable linear correction to the nominal coordinates as a function of time (Table 3).

Our reduction procedure has a number of implications on the derived PSF that are worth mentioning:

- PSFs measured in standard scanmap reductions will typically have a wider core than the recentered ones, due to pointing jitter, possibly imperfect PACS spatial calibration, and potential small synchronisation issues between data and pointing. All of these are tackled ad hoc by the recentering. The last two factors may be reduced in the future with improving calibration while the first will always remain for faint source data to some level. See section 7.2 for a quantitative example. For some of the main Vesta cases we

provide both recentered PSFs, which typically will need observation-specific convolution for application to real data, and PSFs as obtained from normal processing for our particular observation.

- These PSFs represent the convolution of the telescope PSF with the PACS pixel size - PRFs in Spitzer speak. The map pixel is small in comparison to the physical PACS pixel for our adopted parameters.
- Because of redundancy introduced by the scanning, results should be more robust to current incomplete knowledge of reduction steps like flatfield, dubious pixels, crosstalk etc. than chopped/nodded observations. Nevertheless they will be subject to update in case improved flatfields or crosstalk correction methods become available. For v2.0 we already used the v7 photometer flatfield.
- For fast scan and parallel mode, there could be subtle but basic differences between the PSFs derived here from several back and forth scans and using recentering, to the PSF from single pass unidirectional scans as can occur in sparsely sampled maps, because of the effects of detector time response. Section 7.2 suggests these differences are minor.
- By definition of the recentering step, the recentered PSFs will not include ghost related features arising while the source was off the array (e.g., a possible effect of the 'blue streaks' seen for sources just outside the array corner in FM-ILT). See also the discussion of the Mars observations below.

All PSFs presented here are based on the highpass filter / photProject reduction scheme for PACS photometer data. Cross scans for reduction with 'madmap' like inversion algorithms are available for a subset (OD173 Neptune, OD345 Vesta) but have not been used in this way, given the current presence of e.g. artefacts near bright sources in madmap reductions.

5 Results

Figures 1 to 3 show the resulting recentered Vesta PSF images at different linear stretches -0.05–1, -0.005–0.1 and -0.0005–0.01 times the PSF peak. α Tau results are consistent but of lower S/N. The linear noise structures in scan direction are a consequence of the fairly large width highpass filter that was used. It should be noted that at the given noise level, background sources start to be detected and are in fact seen outside the image panels shown. Enough PSF obervations have been obtained in the meantime to make sure that those faint features that are explicitly discussed in this note are not due to background objects or real structures near α Tau or Vesta. The good agreement between the two datasets from different targets is the most obvious evidence.

Table 4 summarizes results from fitting a 2-dimensional Gaussian to the full PSF including wings. While such gaussian fits may not be an optimal representation of the PSF they allow for quick comparison with mapping results from other observations. The PSF width in blue for slow scan is similar to first results that were seen in single frame staring data, giving confidence that the recentering/mapping procedure recovers the actual PACS PSF. The agreement between the widths measured from the Vesta and α Tau datasets is very good.

5.1 PSF morphology

In all three bands the PSF core is surrounded by a tri-lobe pattern at the level of up to 10% (in blue) of the PSF peak. The optical modelling by N. Geis presented in PICC-ME-TN-029 Issue 2.0 reproduces this basic morphology by considering the wavefront errors of the Herschel main mirror. The wavefront errors are reflecting,

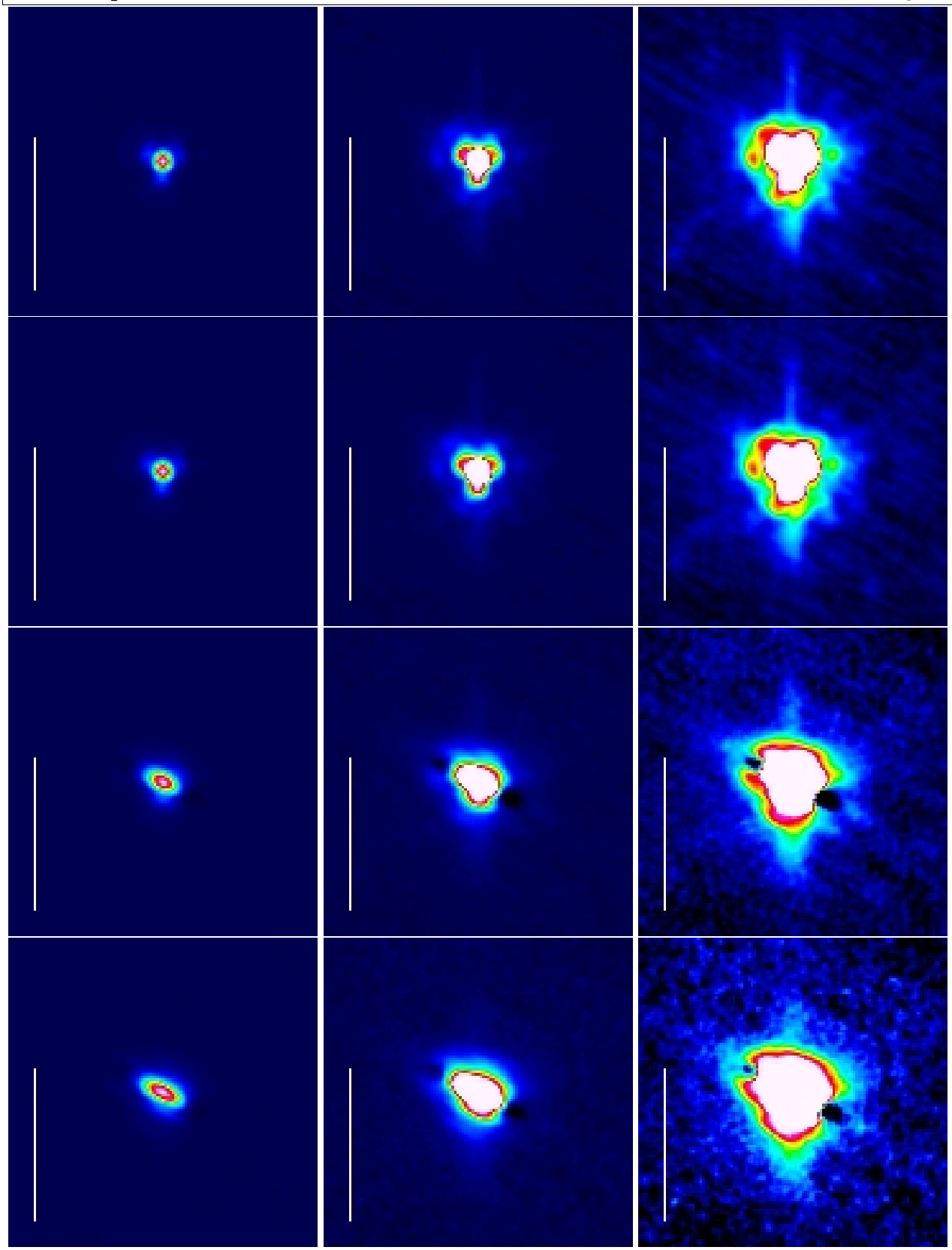

Figure 1: Blue PSF from recentered OD160 Vesta data, from left to right linearly scaled to peak, 10%, and 1% of peak. From top to bottom scanspeed 10 (low), 20 (medium) , 60 arcsec/sec (fast) and (simulated) parallel mode at 60 arcsec/sec. Spacecraft Z is on top as if telescope PA=0. Array-to-map angle (scan direction) is 63deg in instrument coordinates. The scale bar indicates 60arcsec.

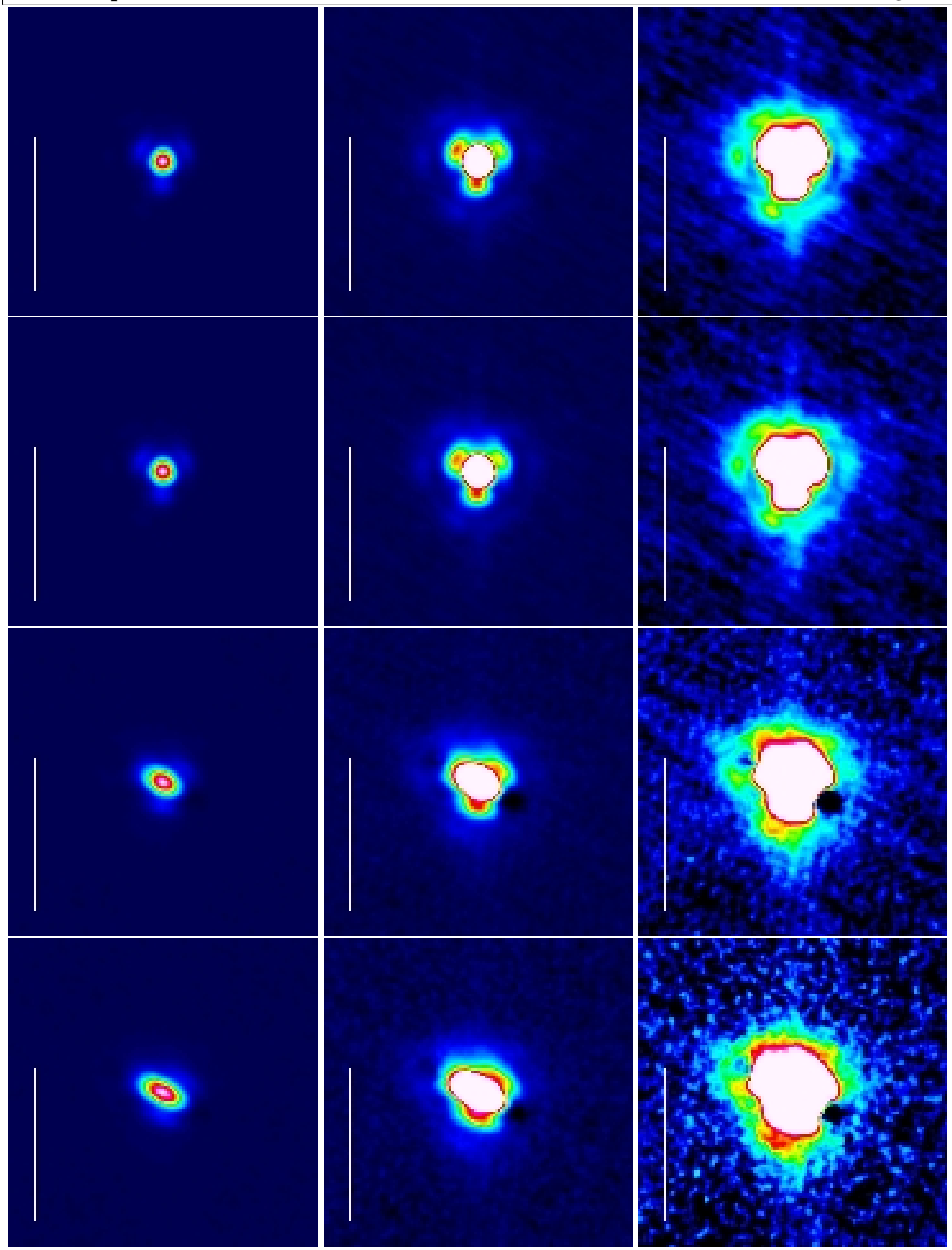

Figure 2: Green PSF from recentered OD160 Vesta data, from left to right linearly scaled to peak, 10%, and 1% of peak. From top to bottom scanspeed 10, 20, 60 arcsec/sec and (simulated) parallel mode at 60 arcsec/sec. The scale bar indicates 60arcsec.

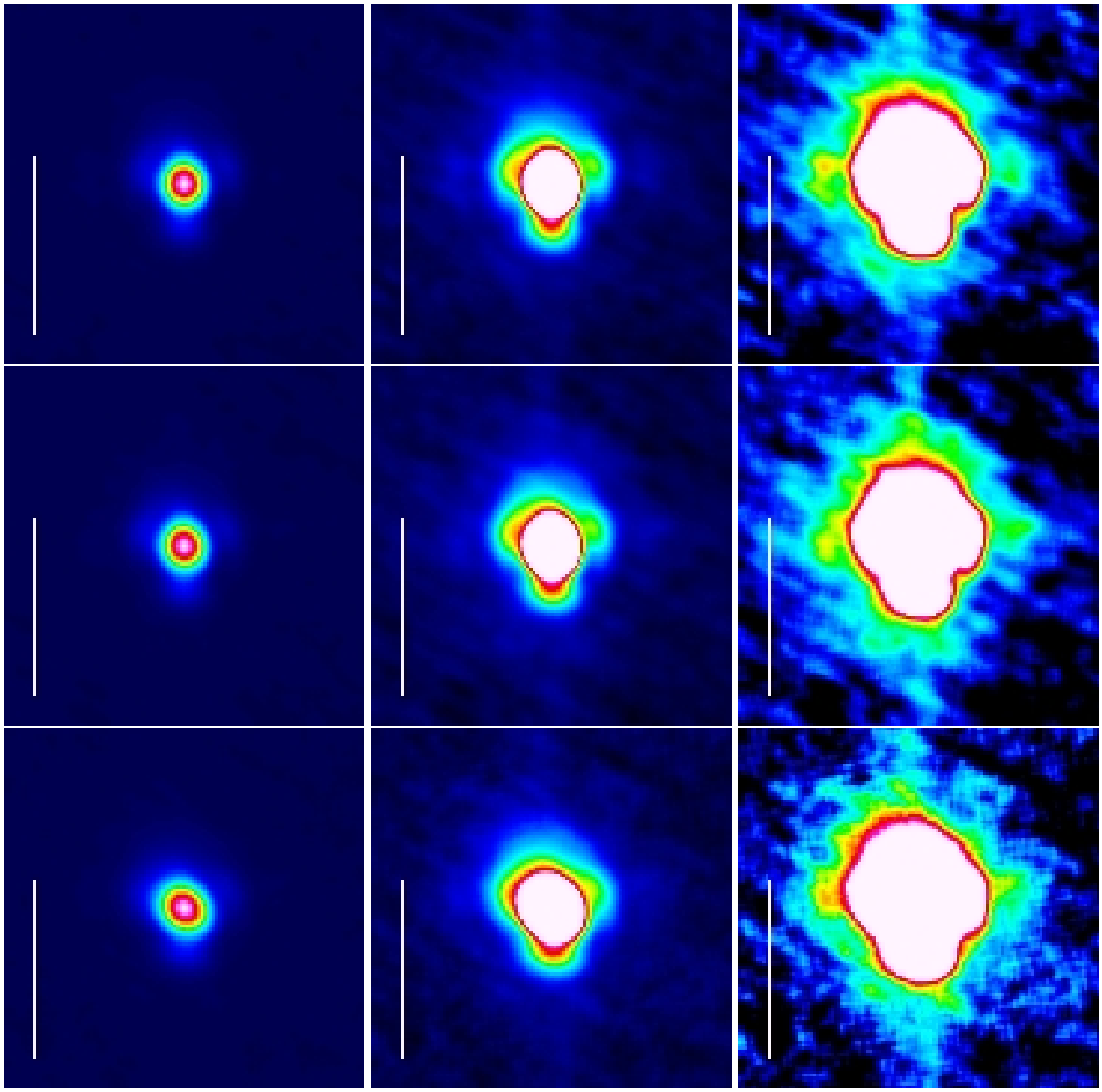

Figure 3: Red PSF from recentered OD160 Vesta data, from left to right linearly scaled to peak, 10%, and 1% of peak. From top to bottom scanspeed 10, 20, 60 arcsec/sec. For red the parallel mode sampling is identical to prime mode. The scale bar indicates 60arcsec.

among other factors, the 120 degree symmetry of the secondary mirror suspensions. In all three bands, the top-right of the three lobes is observed weakest, qualitatively reproduced by the models.

The next fainter level of PSF structures is again not a clear diffraction ring but a knotty pattern at the % level and below. It is clearly seen in blue and well confirmed in the 10 vs. 20 arcsec/sec data. A similar pattern is seen in green but with less detail at current S/N.

The blue data show a weak spike in roughly vertical (spacecraft Z) direction, perhaps similar to a spike seen in ILT data (FM report figure 1.124). The spike is clearly confirmed in green and perhaps also in red. Roughly 70arcsec towards the -Z direction, a bright spot is superposed on this spike, clearly seen in blue and weakly in green (outside the range in Figs 1 to 3). Deeper Vesta and Neptune observations (see below) confirm the bright spot. Results discussed in section 6.4 show it is induced in PACS rather than the telescope, and is likely caused by an optical ghost. The deeper observations also confirm the vertical linear feature, relative to the PSF peak it is strongest and most extended in red. In blue/green it seems shorter and asymmetric, stronger towards the +Z direction (upwards).

The fast scan blue and green PSFs show a region in scan direction from the PSF peak where the flux is undershooting to below zero, to a level of about -1% of the peak. Its origin is not understood, and undershooting of the signal after a short exposure to a bright signal would be needed to create it. It is unclear to which extent this effect is (non)linear. A test reduction using a huge highpass filter width and avoiding deglitching reproduced the effect. The undershoot can already be seen in individual timelines, again demonstrating it is not a processing artefact.

At slow scan speed, the PSF fits are roughly round for blue and green but vertically elongated in the red. This elongation is seen in the PSF core and not just an effect of wings or lobes. A slight elongation in same direction was seen in ILT but cannot be compared quantitatively given the properties of the ILT setup plus its use of somewhat extended holes for the artificial source.

Comparing results for the slower scanspeeds 10 (slow) and 20 arcsec/sec (medium), the PSFs are very similar at both speeds in all bands. Fast scan and in particular blue/green parallel mode with 8-sample averaging show significant elongation in scan direction, as expected. The detailed PSF pattern for fast scan will depend on the relative orientation of scan direction and the tri-lobe pattern. The PSFs shown here can give only examples for the given scan direction relative to the array. Given the SPIRE-driven preference for the 'magic' array-to-map angles +42 and -42deg (instrument coordinates) in parallel mode, dedicated observations were obtained in OD345 at these array-to-map angles, and the results were verified on (lower S/N) true parallel mode observations of αBoo taken in OD269. Table 5 gives width results for these array-to-map angles. Figure 4 shows examples.

5.2 PSF in SPIRE/PACS Parallel mode

In parallel mode, PACS maps are formed from the combination of scans at array-to-map angle +42 and -42 degree, taken at 60arcsec/sec or 20arcsec/sec speed. The PSF of each scan is elongated in scan direction, with undershoots after source passage (Sect. 5.1). Blue or green data are averaged over 8 rather than 4 samples which further increases the elongation.

Fig. 5 shows parallel mode PSFs constructed by coadding OD345 'simulated parallel mode' Vesta data taken

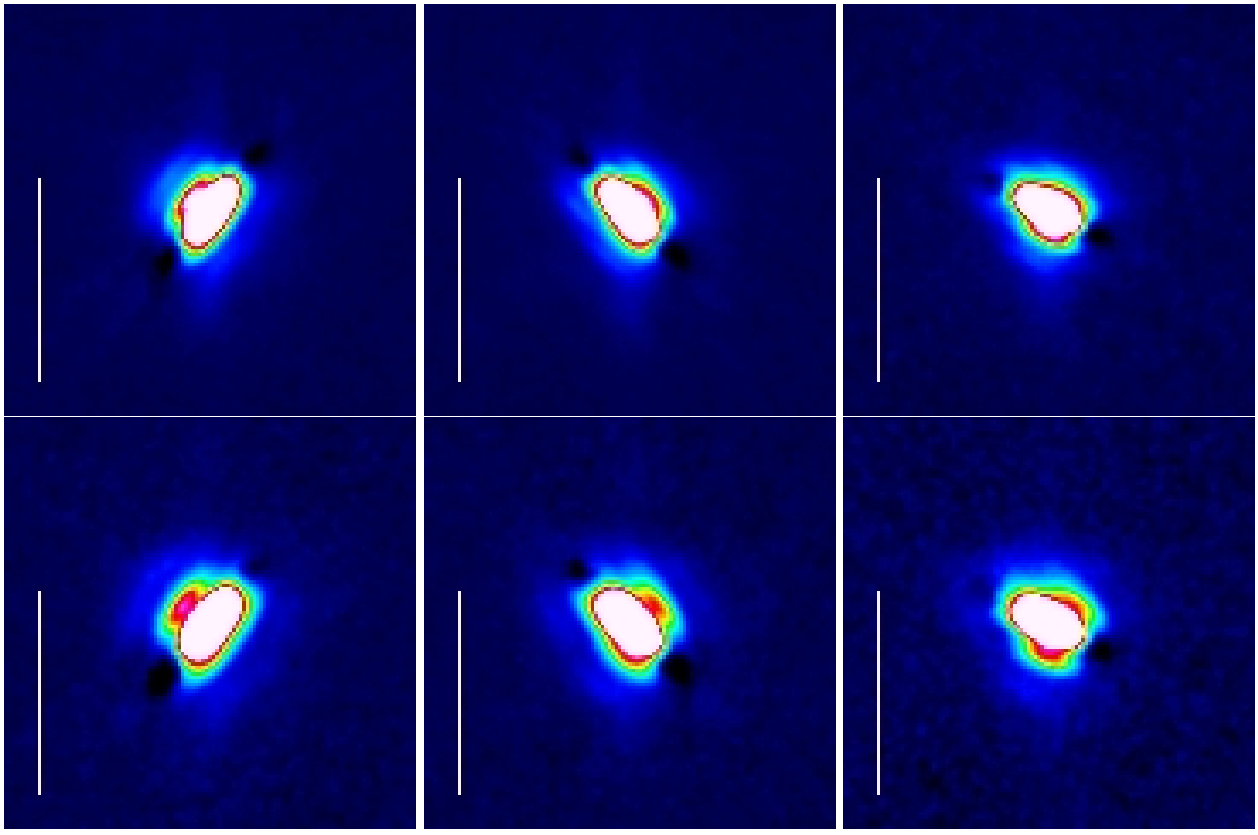

Figure 4: Example of the effect of scan direction on the PSF, shown here for fast parallel mode blue (top) and green (bottom) and the three array-to-map angles -42, +42, +63degree from left to right. The alignment of true PSF features and scan smearing changes.

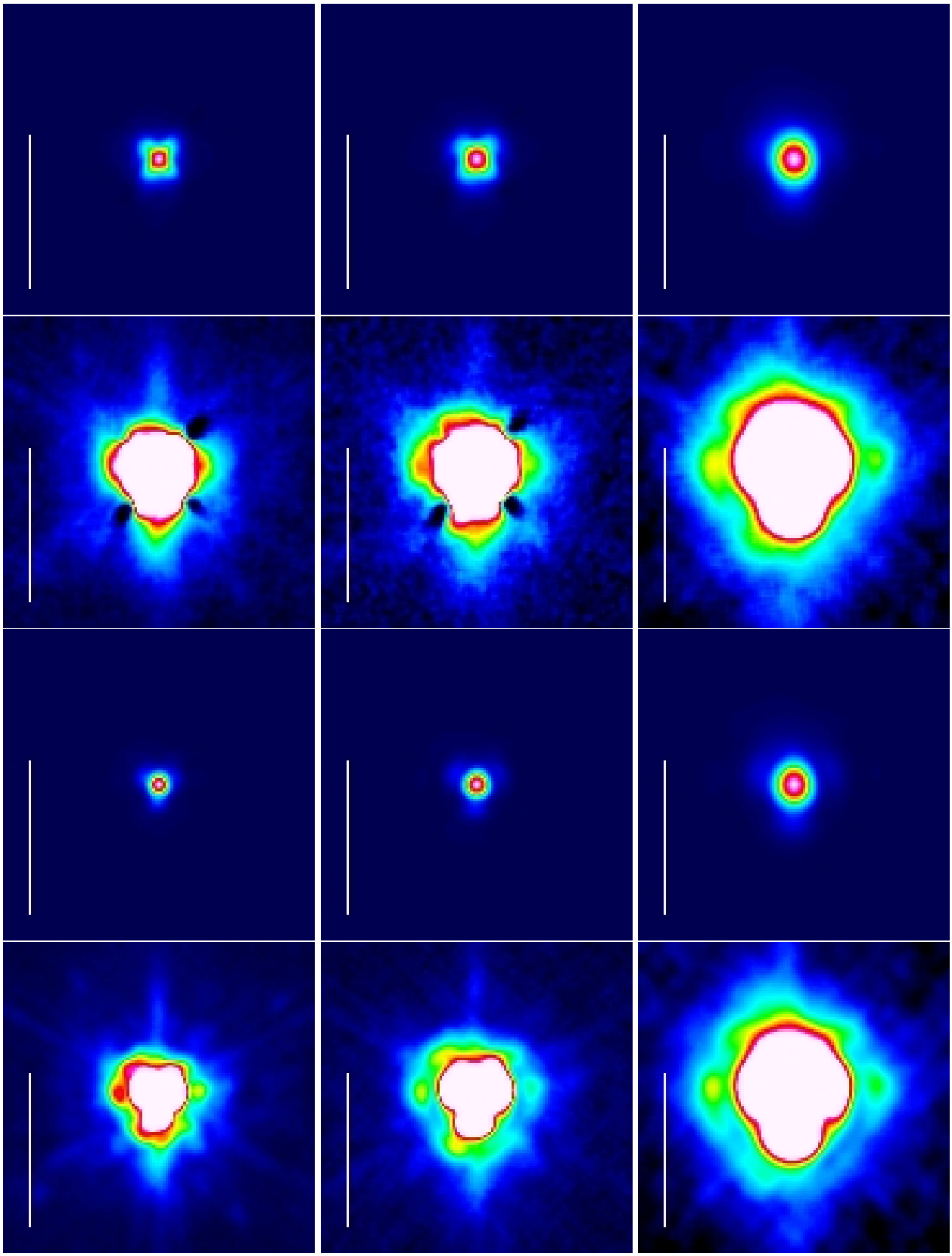

Figure 5: PSF in parallel mode, for sources crossed at array-to-map angle +42 and -42 and forth and back. From left to right: blue, green, red. From top to bottom: Speed 60arcsec/sec scaled to peak, speed 60arcsec/sec scaled to 1% of peak, speed 20arcsec/sec scaled to peak, speed 20arcsec/sec scaled to 1% of peak.

Band	Speed arcsec/sec	FWHM arcsec Vesta OD160	PA deg	FWHM arcsec αTau OD118	PA deg
Blue	10	5.20×5.56		5.21×5.57	
Blue	20	5.41×5.72		5.41×5.71	
Blue	60	5.70×9.05	61.7	5.70×8.92	61.7
Blue	20/para	5.52×6.28	53.6		
Blue	60/para	5.80×12.06	62.5		
Green	10	6.54×6.78		6.52×6.75	
Green	20	6.66×6.89		6.64×6.84	
Green	60	6.84×9.81	61.8	6.84×9.64	61.8
Green	20/para	6.73×7.30	52.8		
Green	60/para	6.93×12.61	62.6		
Red	10	10.38×11.97	6.1	10.41×12.00	8.4
Red	20	10.55×12.08	9.1	10.57×12.05	9.7
Red	60	11.39×13.37	41.2	11.35×13.32	40.9

Table 4: Results of fitting 2-dimensional gaussians to the recentered PSF for Vesta and αTau. Note these are fits to the full PSF including the lobes/wings. Position angles (east of the spacecraft Z direction) are listed only for beams with clearly elongated core. *Array-to-map angle is 63deg in instrument coordinates for these observations.*

Band	Speed arcsec/sec	FWHM arcsec	PA deg	ama deg	OD
Blue	20/para	5.44×6.51	30.8	+42	345
Blue	60/para	5.85×12.58	43.7	+42	345
Green	20/para	6.62×7.44	31.1	+42	345
Green	60/para	6.99×13.15	43.9	+42	345
Red	20	10.29×12.20	8.5	+42	345
Red	60	10.90×14.09	27.7	+42	345
Blue	20/para	5.31×6.68	-26.5	-42	345
Blue	60/para	5.69×12.74	-36.9	-42	345
Green	20/para	6.53×7.56	-27.0	-42	345
Green	60/para	6.87×13.41	-37.1	-42	345
Red	20	10.37×12.27	-3.4	-42	345
Red	60	11.01×14.53	-23.7	-42	345
Blue	20/para	5.52×6.28	53.6	+63	160
Blue	60/para	5.80×12.06	62.5	+63	160
Green	20/para	6.73×7.30	52.8	+63	160
Green	60/para	6.93×12.61	62.6	+63	160
Red	20	10.55×12.08	9.1	+63	160
Red	60	11.39×13.37	41.2	+63	160

Table 5: Results of fitting 2-dimensional gaussians to the recentered PSF of Vesta for the two parallel mode 'magic' array-to-map angles. OD160 results for array-to-map angle +63 are repeated for completeness.

at array-to-map angle +42 and -42 degree. True parallel mode data of αBoo from OD269 are consistent but have lower S/N. The most salient feature is the cross like PSF core seen in blue and green for fast scan speed, due to the equal weight addition of elongated PSFs from the two different scan directions. The red PSF at fast speed does not show a cross-like structure but is still somewhat broadened. At speed 20arcsec/sec, differences to the prime mode PSF are subtle even for blue and green and not obvious in this figure. Table 6 lists basic PSF width and elongation parameters for such parallel mode scan/crossscan coadds.

The effects of fast scan speed, in combination with variations in coverage by scan and cross-scan that will naturally occur in Herschel maps, make the parallel mode PSF more variable within a map, especially for the blue and green filters. The 'crosses' seen in Fig. 5 top occur for positions with similar coverage of scan and cross-scan. If one of them has much less coverage e.g. at the edge of the map, one direction of the cross will dominate. Similarly, the symmetry of the 'undershoots' seen for example in Fig. 5 (second row from top) will reflect not only the array-to-map angle, but also the scan direction. For the highly redendant data used for Fig. 5, the source is crossed in both scan directions for a given array-to-map angle. In a less redundant typical parallel mode observation, many spots on sky will be passed only in one direction for a given array-to-map angle, and hence show the undershoot only on one side. Other spots on sky will be passed both in forward direction and back.

Band	Speed arcsec/sec	FWHM arcsec	PA deg	ama deg	OD
Blue	60/para	8.80×9.60	-4.4	+42, -42	345
Blue	20/para	5.74×6.26	0.4	+42, -42	345
Green	60/para	9.73×10.69	-3.8	+42, -42	345
Green	20/para	6.98×7.42	-2.9	+42, -42	345
Red	60	11.51×13.65	5.3	+42, -42	345
Red	20	10.46×12.27	3.1	+42, -42	345

Table 6: Results of fitting 2-dimensional gaussians to the non-recentered PSF of Vesta. for equal weight of the two parallel mode 'magic' array-to-map angles +42 and -42.

5.3 PSF morphology at faint levels

αTau and Vesta are selected to be bona fide PSF sources: Effectively pointlike at PACS resolution, and having no surrounding far-infrared structure. They are still faint enough to not induce strong nonlinearities or saturation in the bolometer response. Conversely, they are not bright enough to reveal the faintest PSF levels, and simply integrating longer will pose a danger of detecting additional fainter background sources. Figures 6 to 9 present observations of Vesta (using a longer integration than presented above), Ceres, Neptune and Mars. These will reveal progressively fainter PSF detail or straylight effects compared to the PSF core, but the Mars observations are already fully saturated in the center.

For this reason, scanmaps of Mars (OD137, parallel mode, OD888, prime mode with varying scan direction) and Neptune (OD173, scanmap) were inspected only for faint PSF details. Both objects being SSOs without associated nebulosity, they may nevertheless be useful as a reference for other bright source observations. Note that Neptune's brightest moon Triton may reach about 0.5Jy in the blue PACS band but should be in the inner part of the PSF, at radius $\leq$15arcsec.

It should be noted again that some of the features (ghosts, crosstalk) will show up at different levels, depending on which region of the array and of the instrument was crossed by the source in the particular observation, and how exactly the data were reduced. We illustrate this in Figure 11 using the example of the blue Vesta data already shown above. The left panel shows a map from the PSF analysis, using only frames with the source centered within a matrix by some margin, and recentering each frame. The middle panel shows a different reduction, using all data (including the crosstalk affected column of each matrix) and, for illustration purposes, more relaxed deglitching settings. Differences between the two images are: (1) the expected slight global shift of the psf core due to the use of recentering or not. (2) the presence of a negative crosstalk signature in the normal processing, because the frames where the source is centered on crosstalking pixels are included, because the affected columns are kept, and because deglitching is relaxed enough to let pass these events. Different deglitching methods and parameters can weaken this feature again. (3) a weak diagonal excess emission related

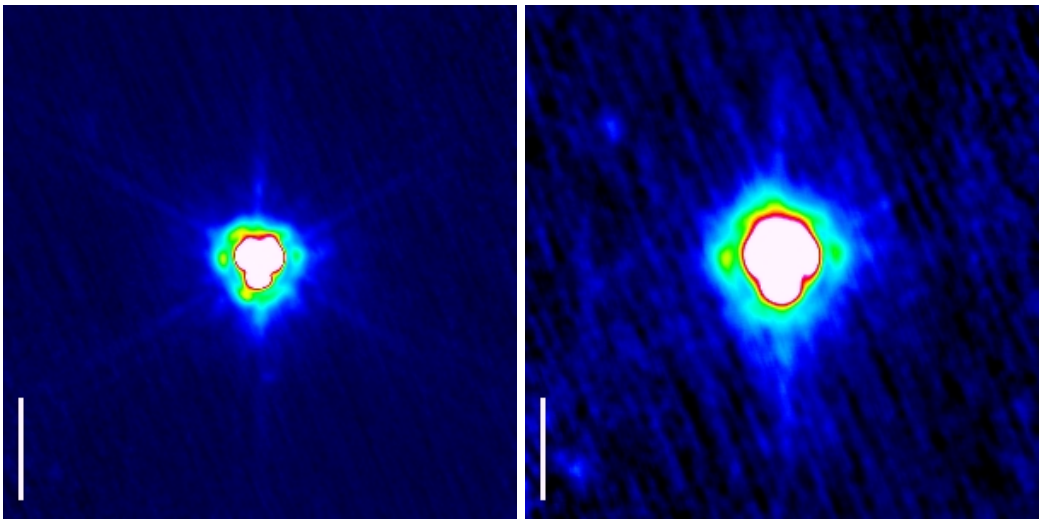

Figure 6: Deep Vesta observations from OD348, left green, right red. Scaling is between -0.0005 and 0.01 of the PSF peak. Comparison to the Ceres and Neptune observations suggests that the two objects to the top and bottom left may be background objects rather than PSF features. Scalebar length is 60arcsec.

to the 'blue streak' ghost feature occuring with the source just outside the corner of the blue array (See FM-ILT report and Section 6.4).

Neptune observations confirm the features seen in Vesta. At this flux level, a processing (not shown in figure) that does not mask the crosstalking columns but with normal deglitching clearly detects a dark spot in the +Y detection, at a separation differing in blue/green vs. red and clearly originating in crosstalk effects (see also PICC-ME-TN-034). Note that the detectability of the spot is a clear function of the deglitching procedure used, like the source itself it may be 'deglitched away' if blindly applying parameters suited for faint source fields.

Very weakly indicated in the Neptune maps are possible linear structures, elongated in Z direction and offset by roughly multiples of matrix sizes in Y direction. Similar features are indicated in the coadditions of many Vesta datasets as well as in certain Key Programme science observations of bright stars. The offsets from the source which are are about commensurate with matrix sizes suggest an origin in PACS by a to be identified mechanism.

The maps of Mars clearly show the 60 degree symmetry multi-spoke pattern expected from the secondary mirror support (see also PICC-ME-TN-029). In all bands, a bright elongated feature crossing the source in scan direction is observed, likely due to an aftereffect on the detector response from passing this extremely bright object. For the OD888 data, this was eliminated in the maps shown by using the redundancy given by four observations with same layout but different scan direction. In the OD137 observations, both blue and red band show a weakly elevated structure, roughly rectangular in spacecraft Y (long side of PACS array) direction, related to the effects discussed in Section 6.

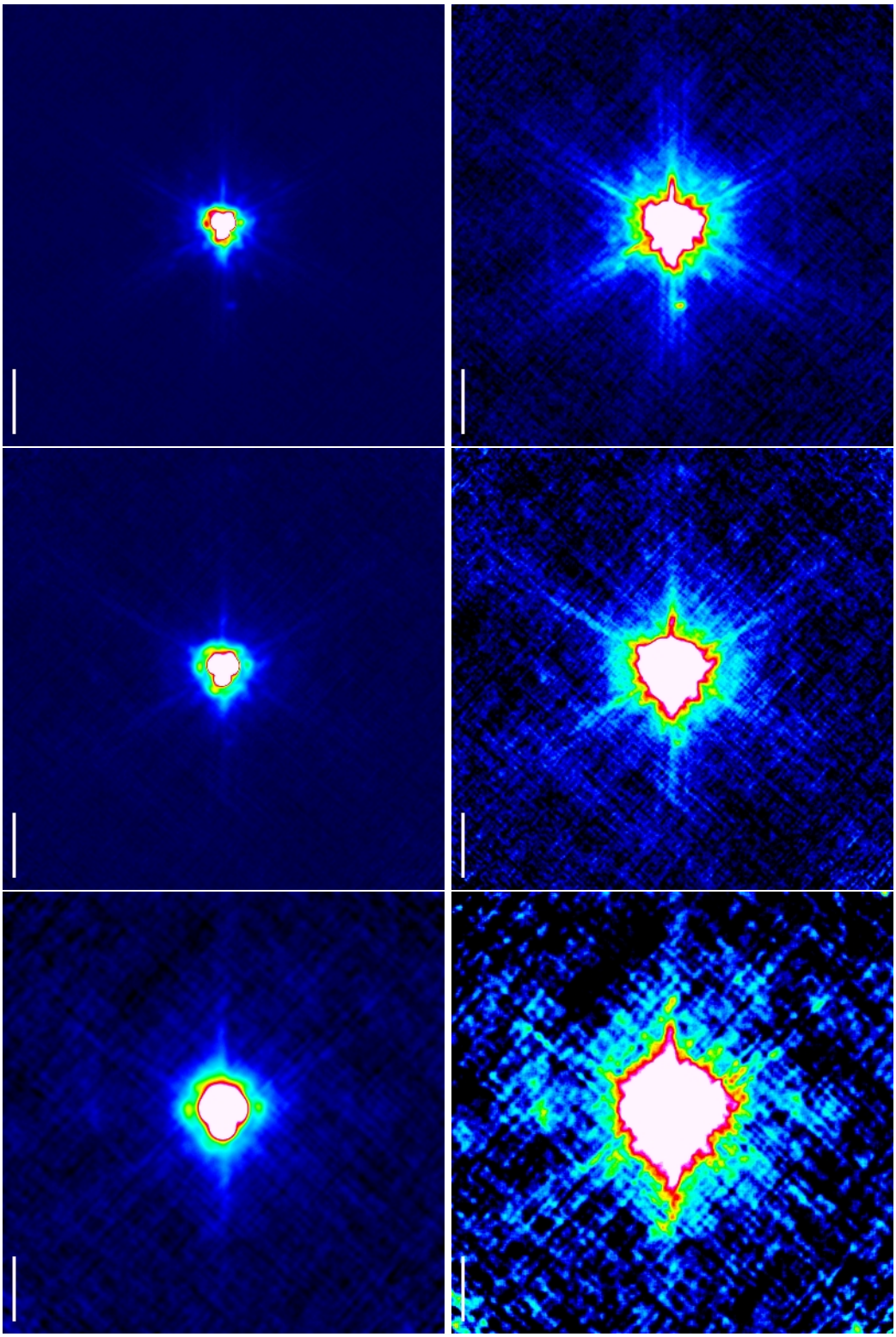

Figure 7: Faint PSF details from scanmaps of Ceres, in blue (top) green (middle) and red (bottom). Maps are averages of two different scan directions 45 and 135 deg and two ODs: 734 and 782. The scale bar indicates 60arcsec. Scaling is between -0.0005 and 0.01 of the PSF peak (left) and -0.00005 and 0.001 of the PSF peak (right).

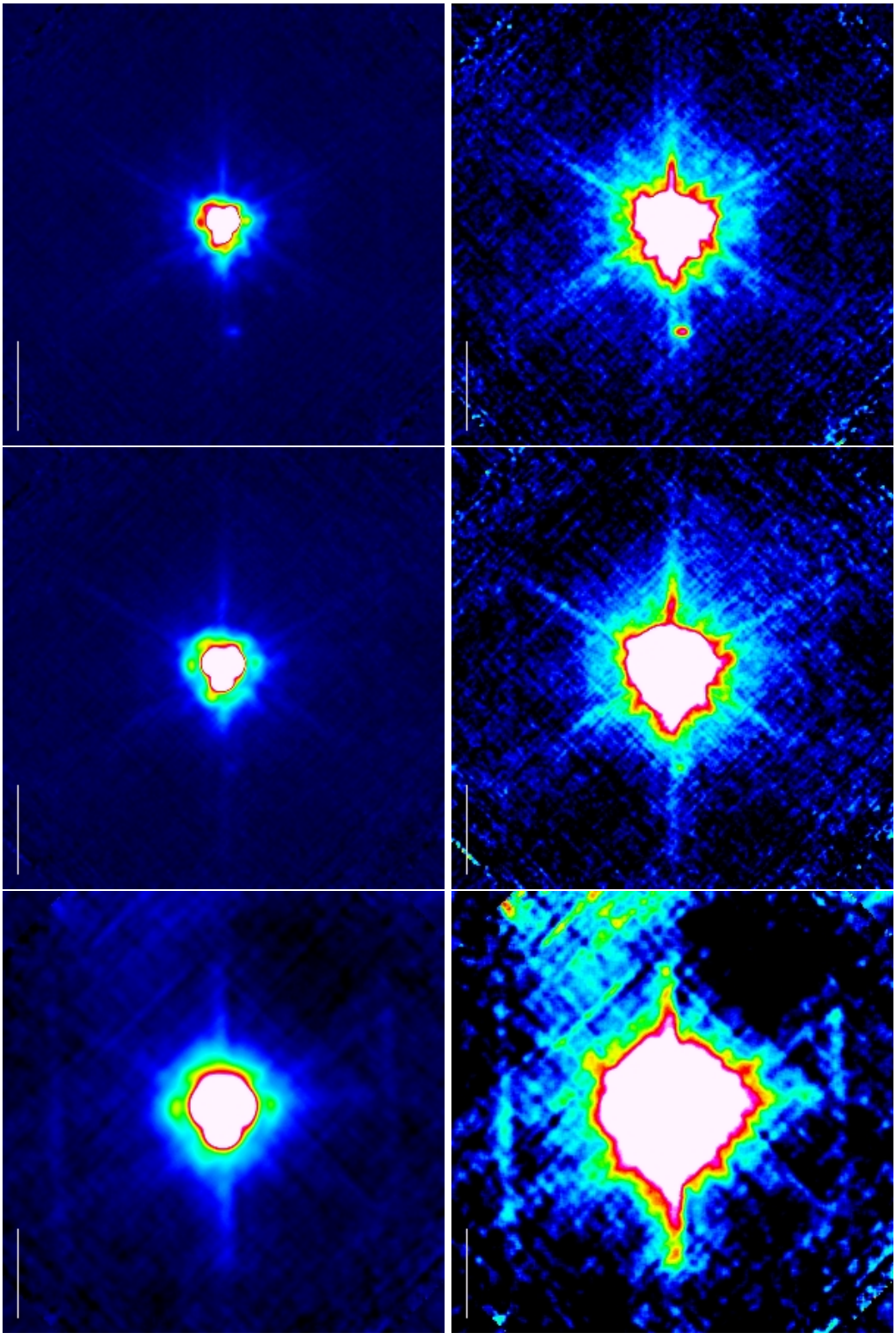

Figure 8: Faint PSF details from scanmaps of Neptune, in blue (top) green (middle) and red (bottom). Maps are averages of two different scan directions 45 and 135 deg. The scale bar indicates 60arcsec. Scaling is between -0.0005 and 0.01 of the PSF peak (left) and -0.00005 and 0.001 of the PSF peak (right).

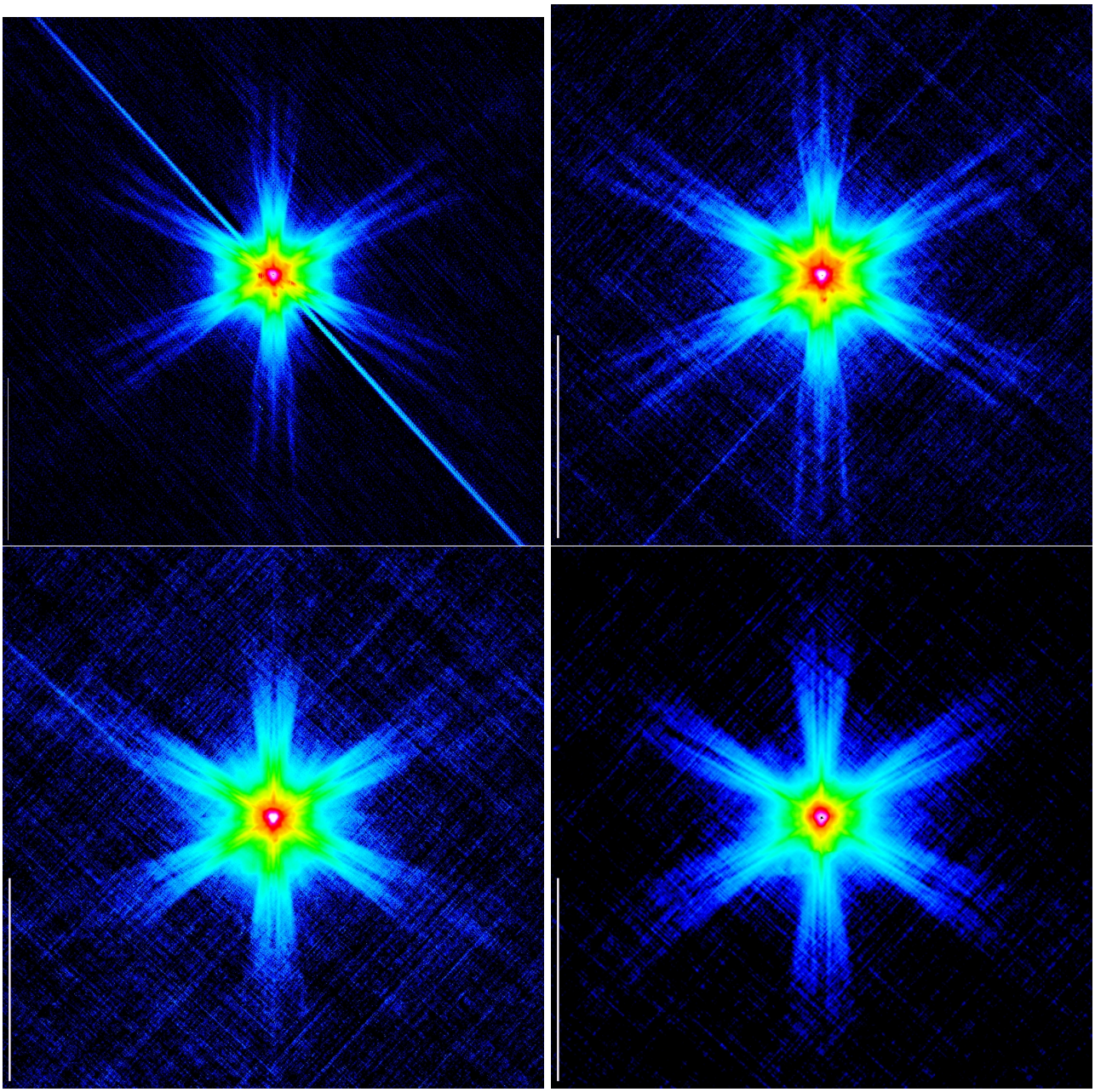

Figure 9: Faint PSF details from scanmaps of Mars. Top left: blue map from OD137, illustrating saturation aftereffects (diagonal trail). The Top right (blue), bottom left (green) and bottom right (red) panels show maps constructed from several OD888 observations, by eliminating regions affected by these aftereffects, as well as occasional background sources. The scalebar indicates 600arcsec.

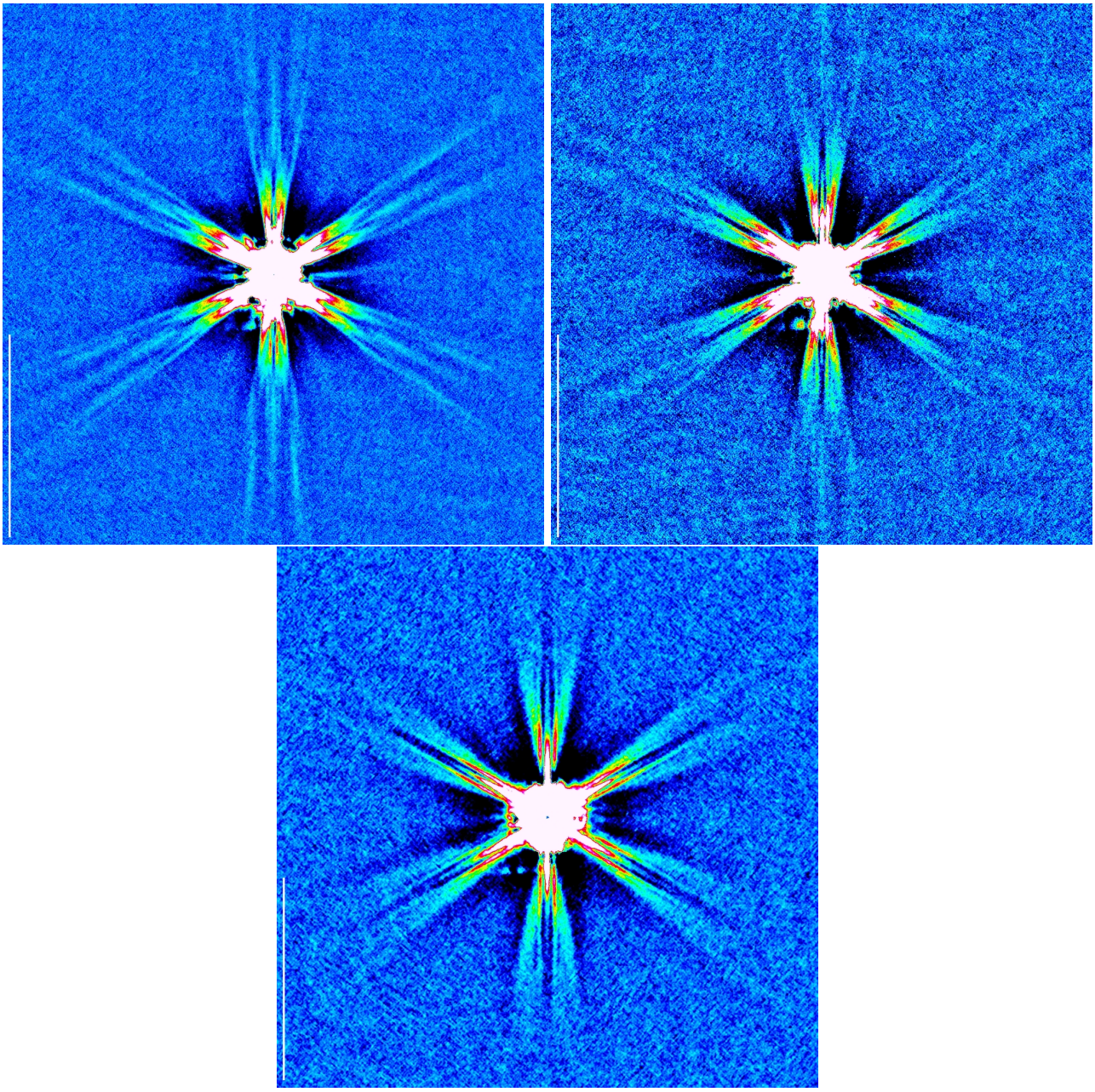

Figure 10: Details of the PSF spikes, based on a reduction of the Mars OD888 maps with reduced filter width and masking. This causes lower noise but severe filter residues near the center. Top left: blue, Top right: green, Bottom: red. The scalebar indicates 600arcsec

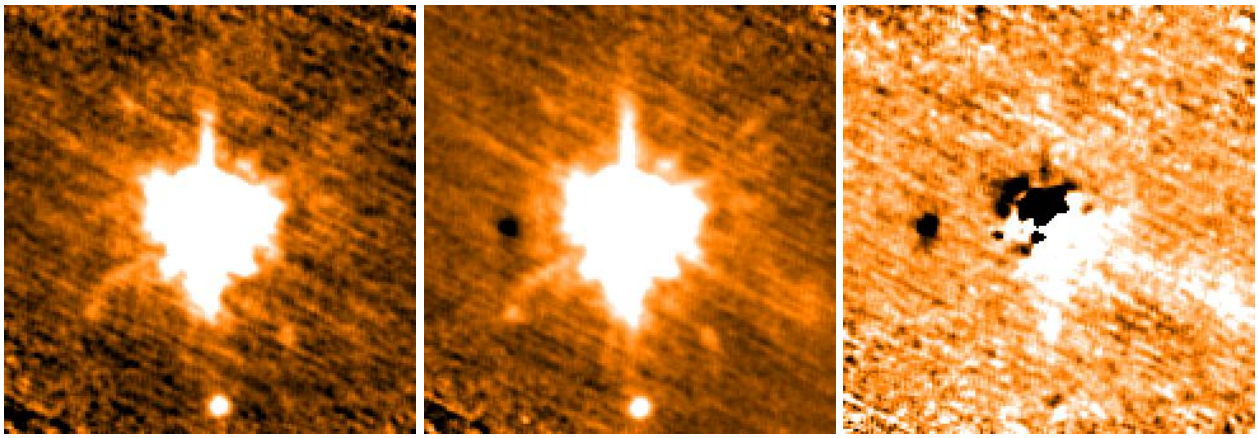

Figure 11: Illustration how mapped area and processing may affect the retrieved PSF. Left: Vesta as processed for the PSF analysis, using recentering. Middle: Normal processing from full AOR and with relaxed deglitching, Right: Difference image.

5.4 Comparison to modelled PSFs

After convolution with the PACS pixel size, the modelled PSFs of PICC-ME-TN-029 for the 'as built' telescope can be compared to the recentered PSFs of Table 4 and Table 9. For a Rayleigh-Jeans slope SED, the models predict a gaussian fit FWHM of 4.7, 6.1, and 9.9 arcsec for blue, green, red with minimal noncircularity. Even the slow speed recentered measured PSFs, where scan related smearing can be ignored, show a roughly 10% larger PSF width (pixfrac=1) and still roughly 5% when comparing the drizzled reductions with small pixfrac=0.1 and the model. Also, the real PSFs show a clear elongation in red, which is not captured by the Herschel model. This may be due to both inaccuracies of the model adopted in PICC-ME-029 and to effects within PACS. As noted, an elongation of the red PSF was already suggested from ILT testing, indicating that this effect may arise within PACS.

Figure 12 shows the models over an image size and flux scaling directly comparable to the Vesta PSFs from Figures 1 to 3. The models reproduce well the observed basic morphology, in particular the tri-lobe appearance. As noted, they fail to reproduce the elongated red PSF. They also do not reproduce in detail the relative strengths of the various PSF knots. Going yet fainter, Figure 13 shows outer regions of the blue and red PSF that can be compared to the Mars observations in Fig. 9. The basic sixfold symmetry is well reproduced but there seems to be a tendency for some of the individual rays in the substructure of each of these six branches being more diffuse in the observation. As an example, consider radii of 5-10 arcmin in the blue PSF. The finite ∼6arcsec size of Mars during the observation may contribute here.

Comparison of the inner few arcmin of the observed (Mars) and modelled PSFs shows a number of discrepancies where the observed PSFs break the six-fold symmetry. One example is the elongation of the observed PSFs in Y direction leading to a more rectangular appearance at the level shown in light blue in Fig. 9 (top left). Another one is the enhanced flux seen at PA∼240deg at radius 1-2arcmin in the blue Mars PSF. We discuss in the next section to which extent they can be explained by ghosts and other PACS peculiarities.

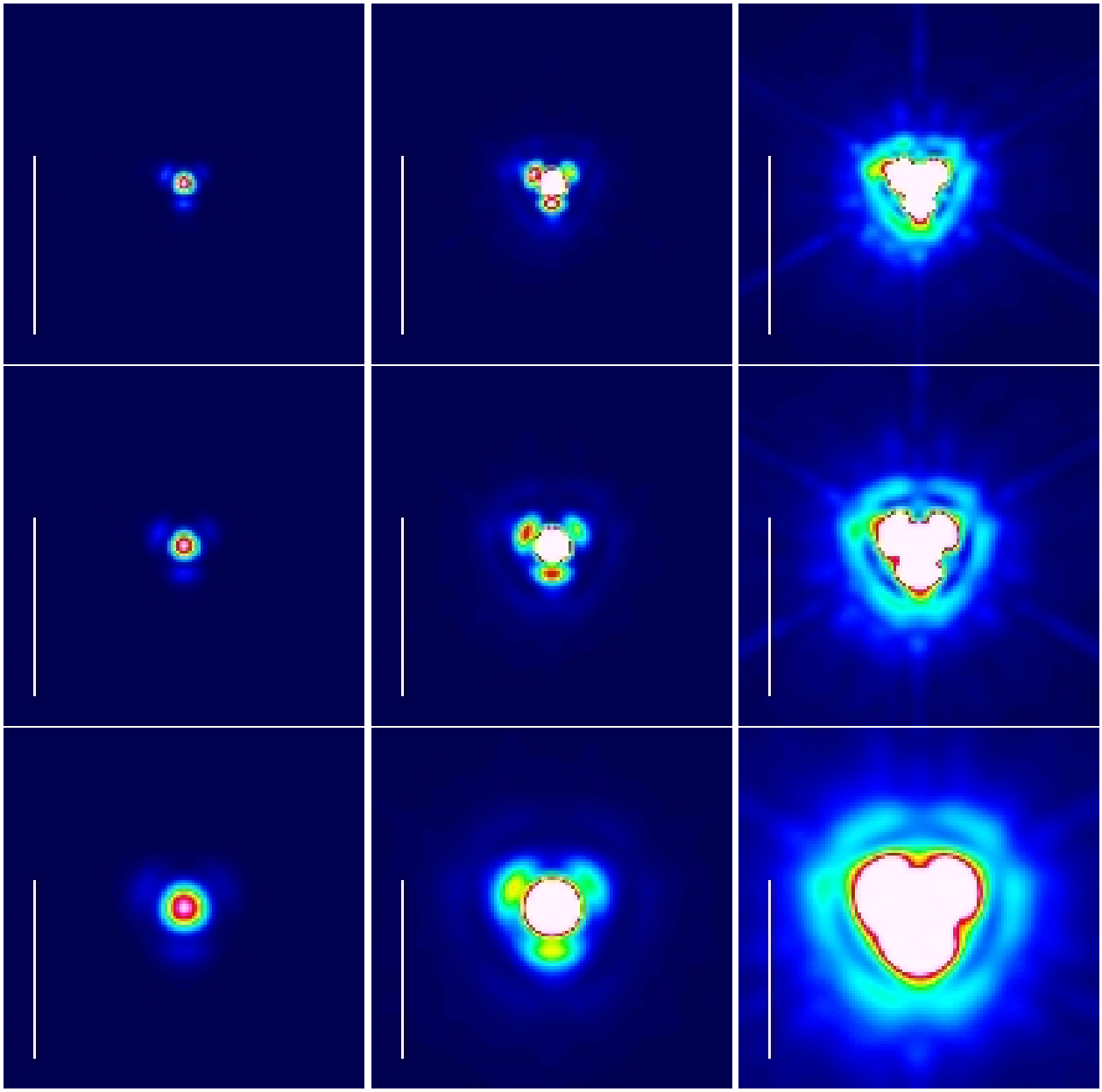

Figure 12: PSF details from model PSFs for a Rayleigh-Jeans source. From left to right linearly scaled to peak, 10%, and 1% of peak. Top: blue, Center: green, Bottom: red. The scale bar indicates 60 arcsec. To be compared to the observed PSFs in the top rows of Figs. 1 to 3.

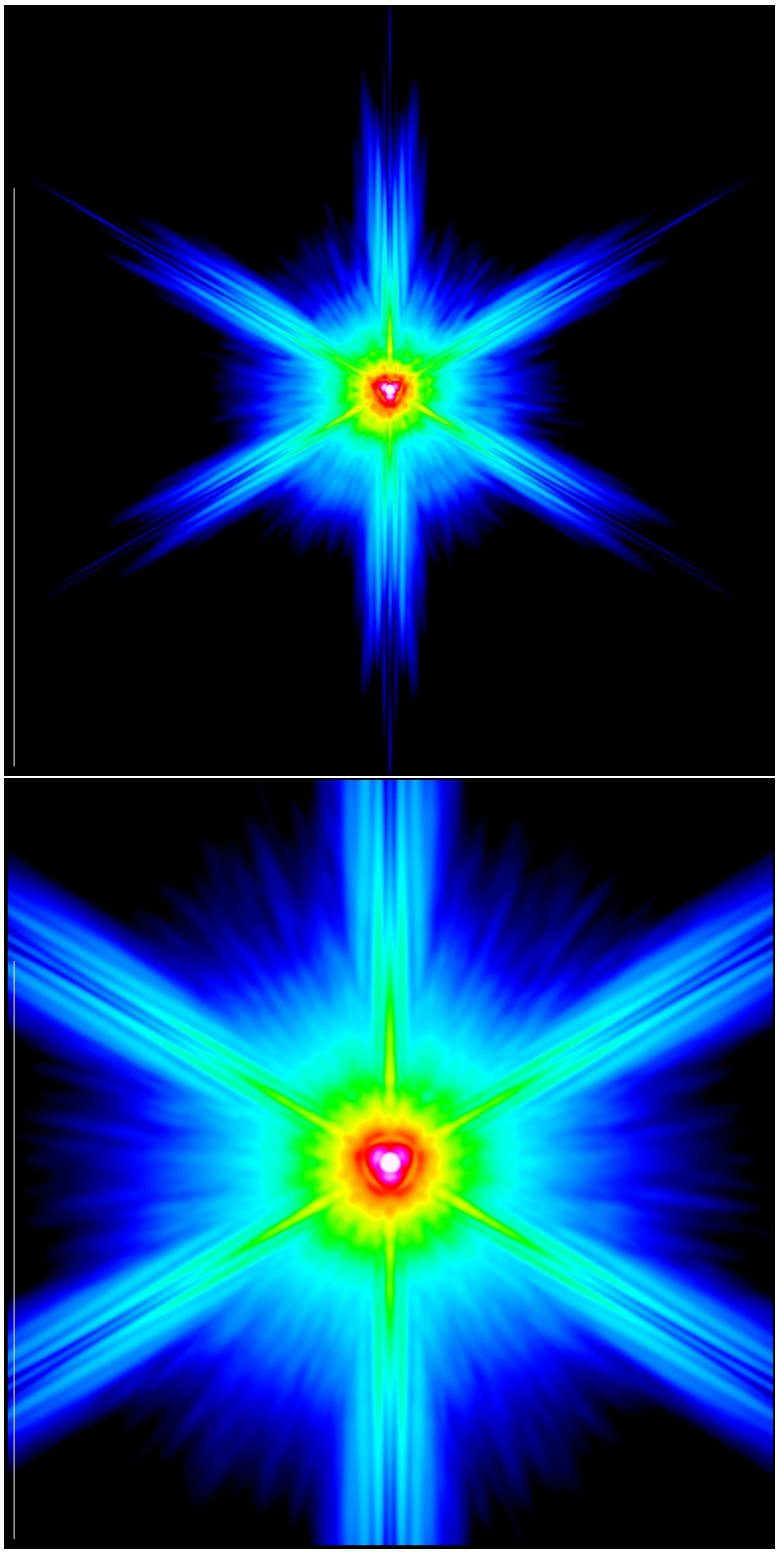

Figure 13: Faint PSF details from model PSFs for a Rayleigh-Jeans source. Logarithmic display. Top: blue, Bottom: red. The scale bar indicates 600 arcsec.

6 Impact of nonlinearity, saturation, crosstalk, ghosts, and straylight on observed PSF

6.1 Nonlinearity

The PACS bolometers respond in a nonlinear way to very bright sources. For point sources this gets noticeable when approaching the 100Jy regime. This behaviour has been characterized in the laboratory (PICC-NHSC-TR-031) and is implemented in the photNonLinearityCorrection task, which was used for the creation of the PSFs released with version 2.0 of this note. Fig. 14 illustrates the effect on the PSF for a very bright source (Ceres OD782): the central peak is too weak in a reduction without nonlinearity correction. Most of the results in this note are based on Vesta data from OD160. Compared to version 1.0 and earlier (when photNonLinearityCorrection was unavailable), we now find for these a PSF FWHM lower by a few hundredths of an arcsec in blue and effectively unchanged in the other bands, leading to an almost perfect agreement with the values for αTau. These effects are small compared to other sources of variation in FWHM (see below).

6.2 Saturation aftereffects

For the observations of Mars, the pixels centered on the source are heavily saturated. While the affected detector pixel comes out of saturation quickly after the source has passed, it does not recover instantaneously to a stable pre-saturation signal. This leads to significant trails in scan direction for the highpass filtered maps shown in the top left panel of Figure 9. See also the saturation aftereffects in the panels of Fig. 21, showing cuts through the arrays as function of time. Because these effects are quite variable in magnitude and sign from pixel to pixel, they interact in a complex way with the mapping and the 2nd level deglitching.

6.3 Detector crosstalk

An electrical crosstalk is observed in the PACS arrays between columns 15 and 0 in the same row within each matrix (see sketch in Fig. 15). The amount of crosstalk depends on the setup of the bolometer control voltages and nonlinearly on source flux (K. Okumura, priv. comm.). For a bright source (V814 Her) and the in-orbit bolometer settings, crosstalk signal in column 0 was typically a few percent of the true signal in column 15 and negative (PICC-ME-TN034). Some red pixels show strong positive crosstalk and are thus excluded by the current bad pixel mask.

Crosstalk will hence induce a negative image that is offset by about 50 arcsec (blue, green) and 100 arcsec (red) towards positive spacecraft Y direction. Its magnitude in a final map will vary, depending on how often the source crossed column 15 (see Fig. 11 for illustration), and on the deglitching methods used which will tend to decrease the magnitude of the effect.

The crosstalk signatures are visible in some figures of this note, specifically Fig. 11 center. In our PA=0 visualisations they are found offset to the left from the source peak.

In datasets where this is possible in terms of S/N and redundancy of the adopted scanning scheme, the crosstalk

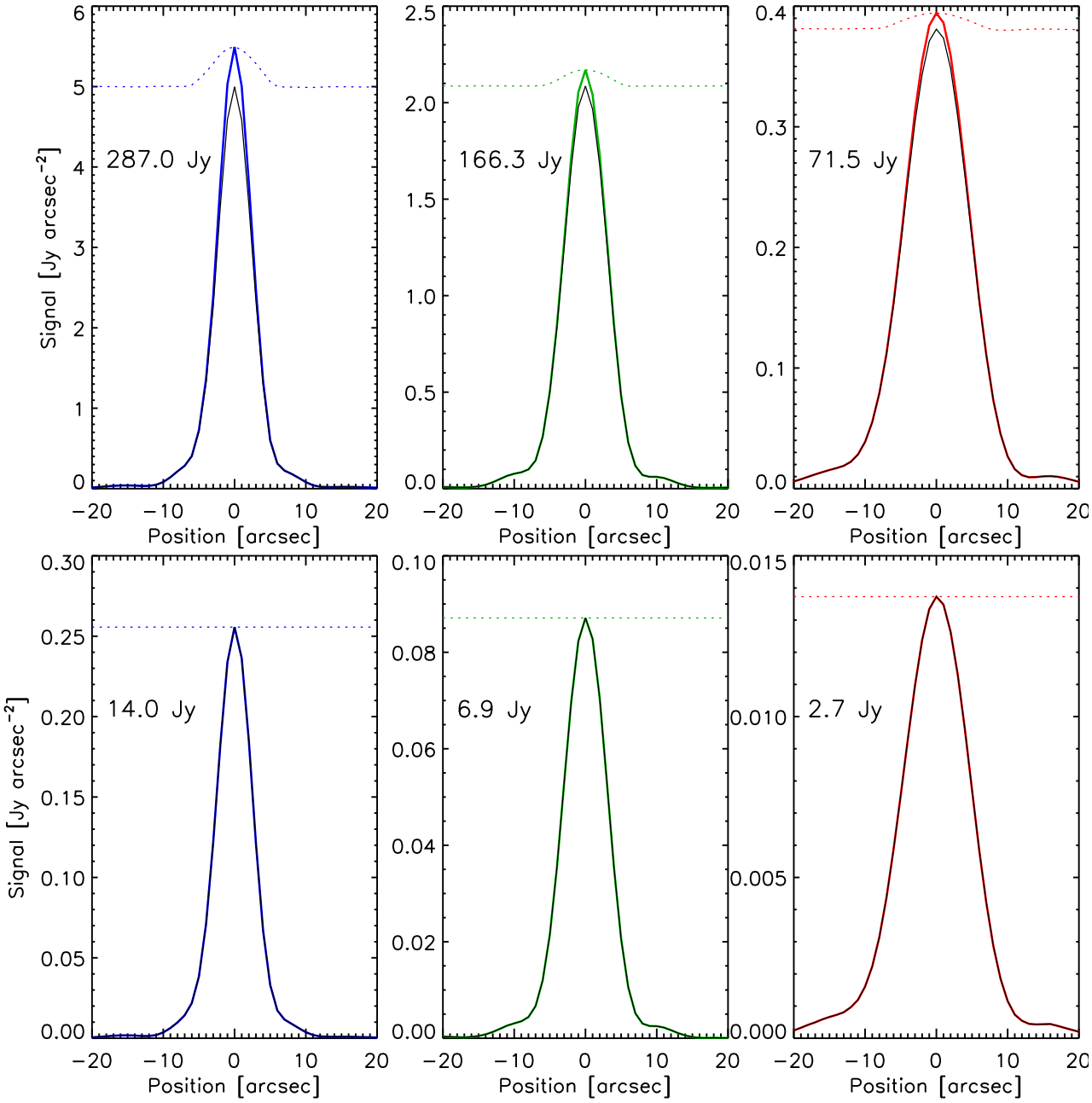

Figure 14: Effect of nonlinearity correction on the PSF for a bright source where such effects are noticeable (Ceres, OD782, top) and a source in the linear regime (αTau, bottom). Shown for the three PACS bands from left to right are cuts through the PSF as corrected for nonlinearity (solid color), uncorrected (black) and ratio of the two (dotted color, multiplied with the peak signal). The total source flux in the given band is also noted.

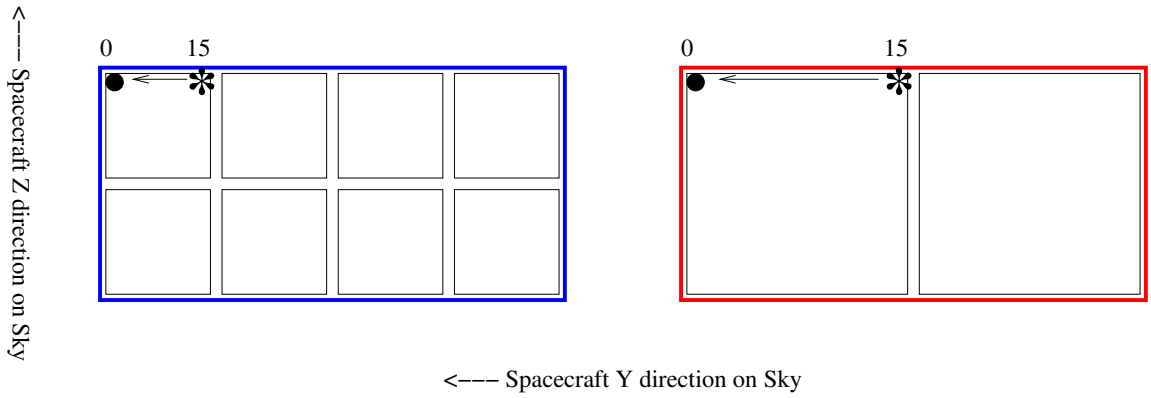

Figure 15: Schematic illustration of crosstalk within the blue and red matrices of PACS. If the source (asterisk) is placed above column 15 of a given matrix, crosstalk effects are seen in the same matrix in column 0 of the same row.

effect on the PSF can be suppressed by excluding the first column of each detector matrix from the analysis. This can be done via the photMaskCrosstalk task, which was applied for creation of the PSFs released with version 2.0 of this note.

6.4 Ghosts in blue array

Section 5.1 noted the presence of a compact blue/green PSF feature offset about 70arcsec in negative Z direction from the PSF peak. Inspection of the Mars data frame by frame shows that this feature is present only if the source itself falls on the array, but not if it has moved off in Z direction by a small amount that would still keep the feature on the array (Figs. 16 and 17). This clearly argues for an origin in PACS rather than the Herschel telescope.

An electrical crosstalk effect would in principle be consistent with this behaviour. We consider it an unlikely explanation, however, because the crosstalk effect would have to occur between different rows of different matrices, and because the different ratio of feature to PSF peak for blue and green (Fig. 8) would need additional nonlinearity as an explanation.

We interpret the feature as an optical ghost, offset from the PSF peak by about -70arcsec in Z and -7arcsec in Y and reaching about 10^{-3} of the PSF peak in blue and 5×10^{-4} in green. No such feature was observed in red. Since the feature will be present only in part of the data, its magnitude can in principle be affected by 2nd level deglitching if the source is extremely bright.

A weaker ghost feature is observed in the blue if a very bright late type star is just at the corner of matrix 4 (Figs. 18 and 19). It is well possible that similar or weaker ghosts occur for yet other source positions and contribute to some of the weak knots in integrated PSFs. Finer mapping of the focal plane with such very bright sources (Mars OD906) can better characterise the incidence.

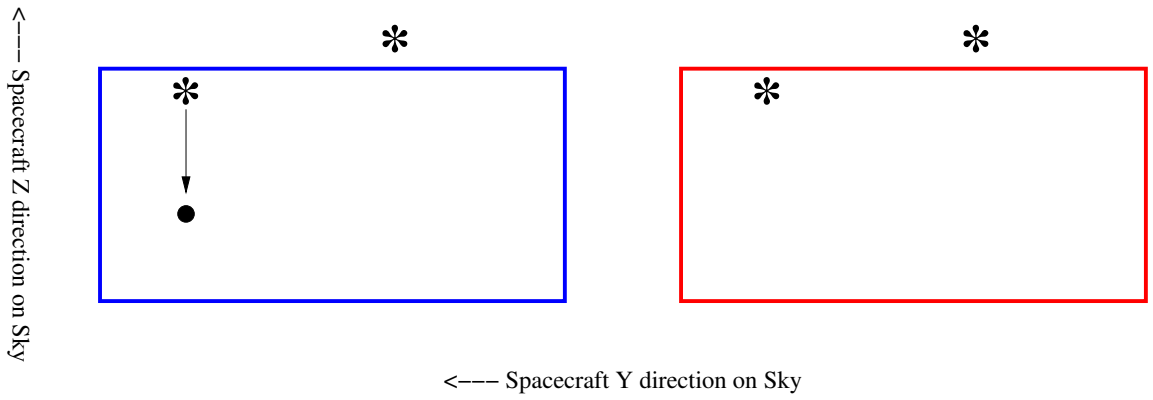

Figure 16: Schematic representation of the compact ghost image seen in blue if a bright source (asterisk) is placed on the array. No ghost is seen with the source off the array. No effect of this magnitude is observed for the red.

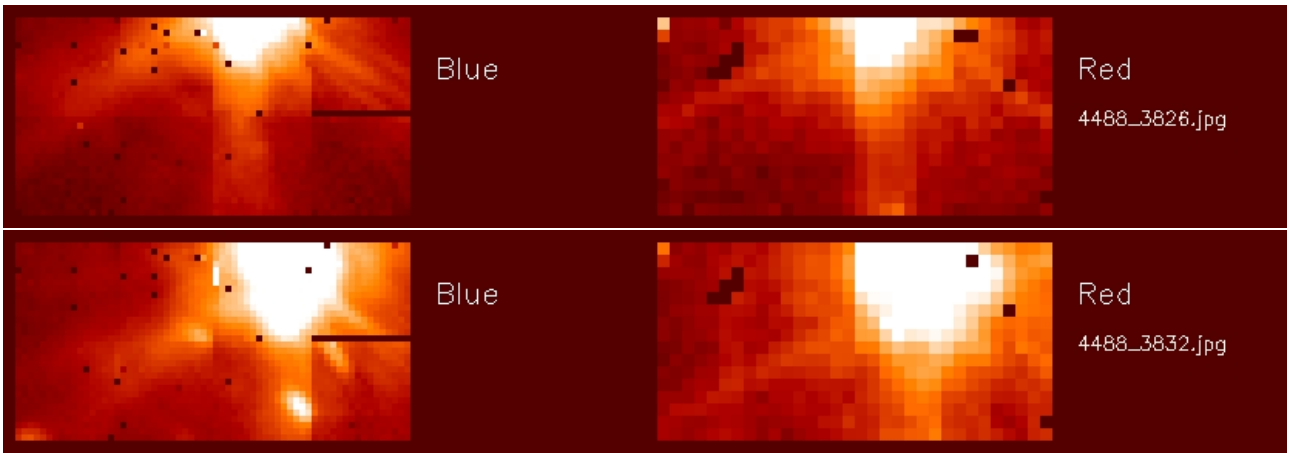

Figure 17: A ghost image on the blue array, shifted about 70arcsec in negative z direction from the true source, is invisible while the source is just outside the array (top) but visible with the source on array (bottom). No such feature is seen in red. Note the weaker features that also don't move with the source, suggesting these are ghosts.

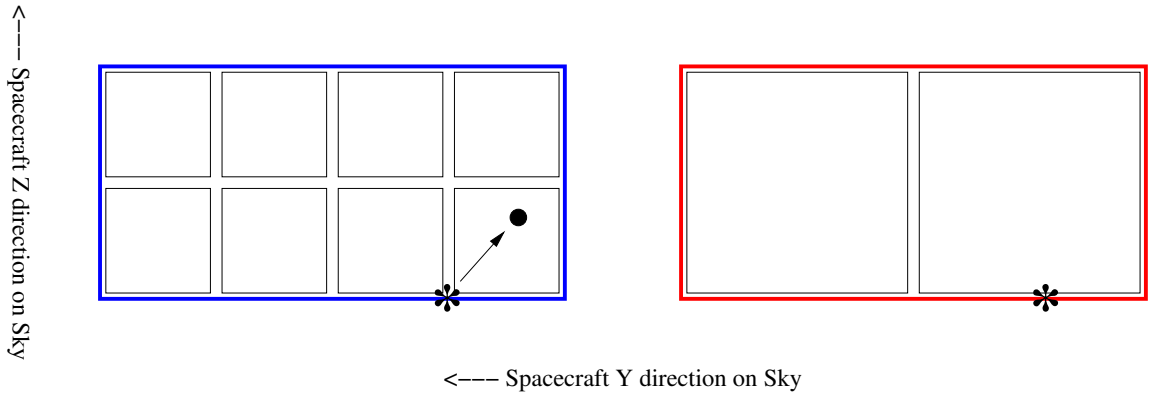

Figure 18: Schematic representation of the compact ghost image seen in blue if a bright source (asterisk) is placed on the corner of matrix 4. No effect of this magnitude is observed for the red. Current data and analysis neither confirm nor exclude similar effects in other matrices.

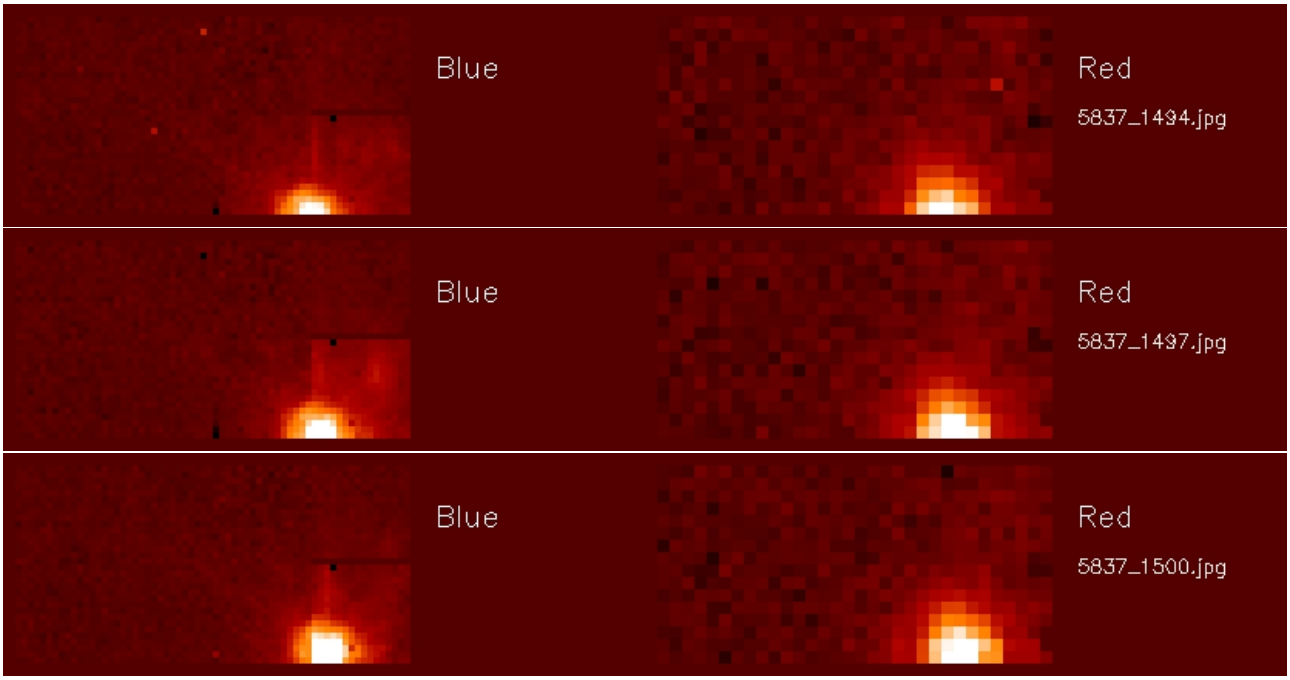

Figure 19: A ghost image on the blue array, shifted about 50arcsec diagonally from the true source across matrix 4 is visible in the middle panel of this sequence. No such feature is seen in red.

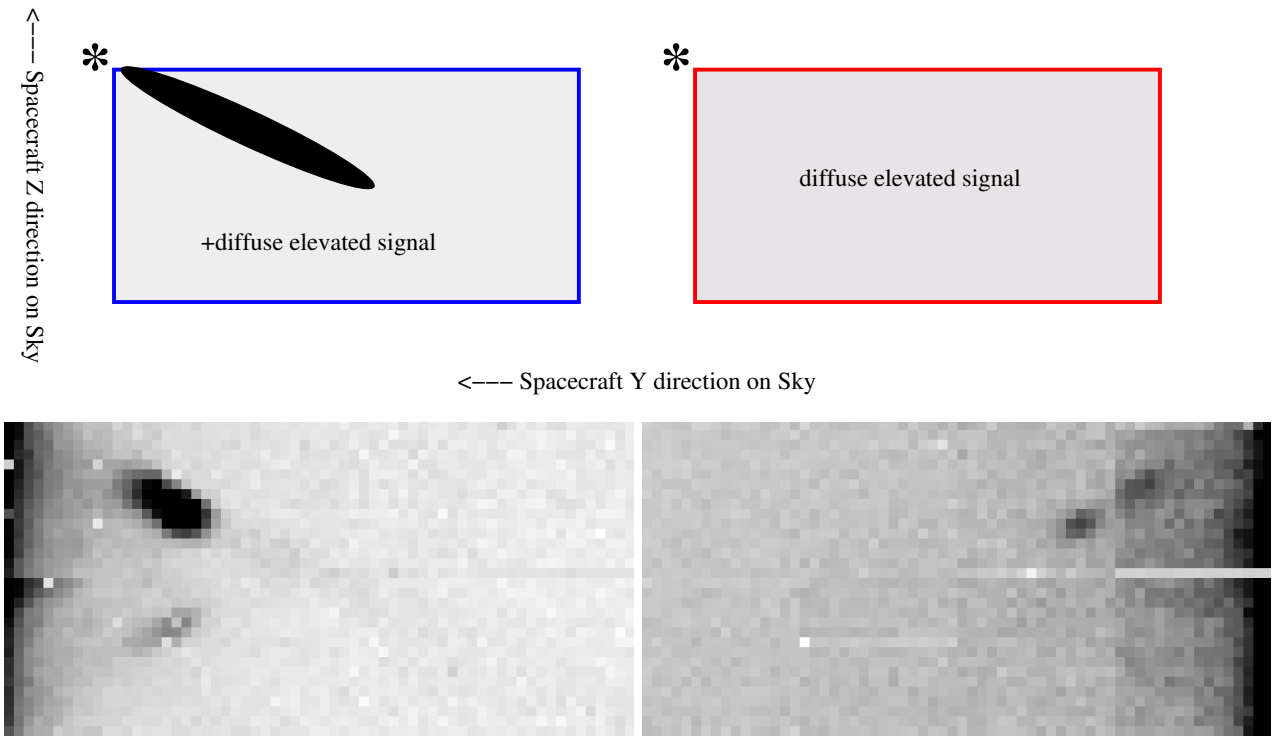

Figure 20: Top: With a bright source placed just outside the top left corner of the blue array, a diagonal 'blue streak' is crossing the array. At the same time, there is a generally elevated signal in blue and in particular red. Bottom: Similar but weaker streaks are seen with sources outside the other corners of the blue array. The two panels show ILT results using the extended PACS internal calibration source just outside the blue field of view.

6.5 Blue streaks, other reflections and straylight effects

A number of peculiar effects are observed while very bright sources are just outside the limits of the array(s). For some of them the morphology clearly suggests an origin in reflections/ghosts off the PACS structure, in other cases direct optical as well as other explanations appear possible.

The brightest of these phenomena are the diagonal 'blue streaks' already observed during ILT, with point sources just outside the blue array corners. They are strongest for the top left corner (Figs. 20 and 21). During the peak of the event these can reach up to about 4% of the source peak (PACS FM-ILT report). In a real map this will be diluted by other PACS pixels having seen the same spot on the sky without being affected. The amount of this dilution will be a function of AOR layout and specific source position. Second level deglitching may change the result further. For the Mars OD137 blue map (Fig. 9 top left) the streak is clearly seen but finally at the 10^{-3} level compared to the peak, and obviously affected by deglitching.

Similar but less pronounced effects have been observed with sources at the edges of the red array, producing linear streaks that extend in vertical or (weaker) horizontal direction (Fig. 22). Inspection of neighbouring red frames as well as of the blue channel shows these again are localized effects rather than general PSF features. The vertical feature in Figure 22 reaches maximal intensity (at a location close to the opposite array edge) of about 1% of the PSF peak, the weaker horizontal one stays around the 10^{-3} level. Both numbers refer to the

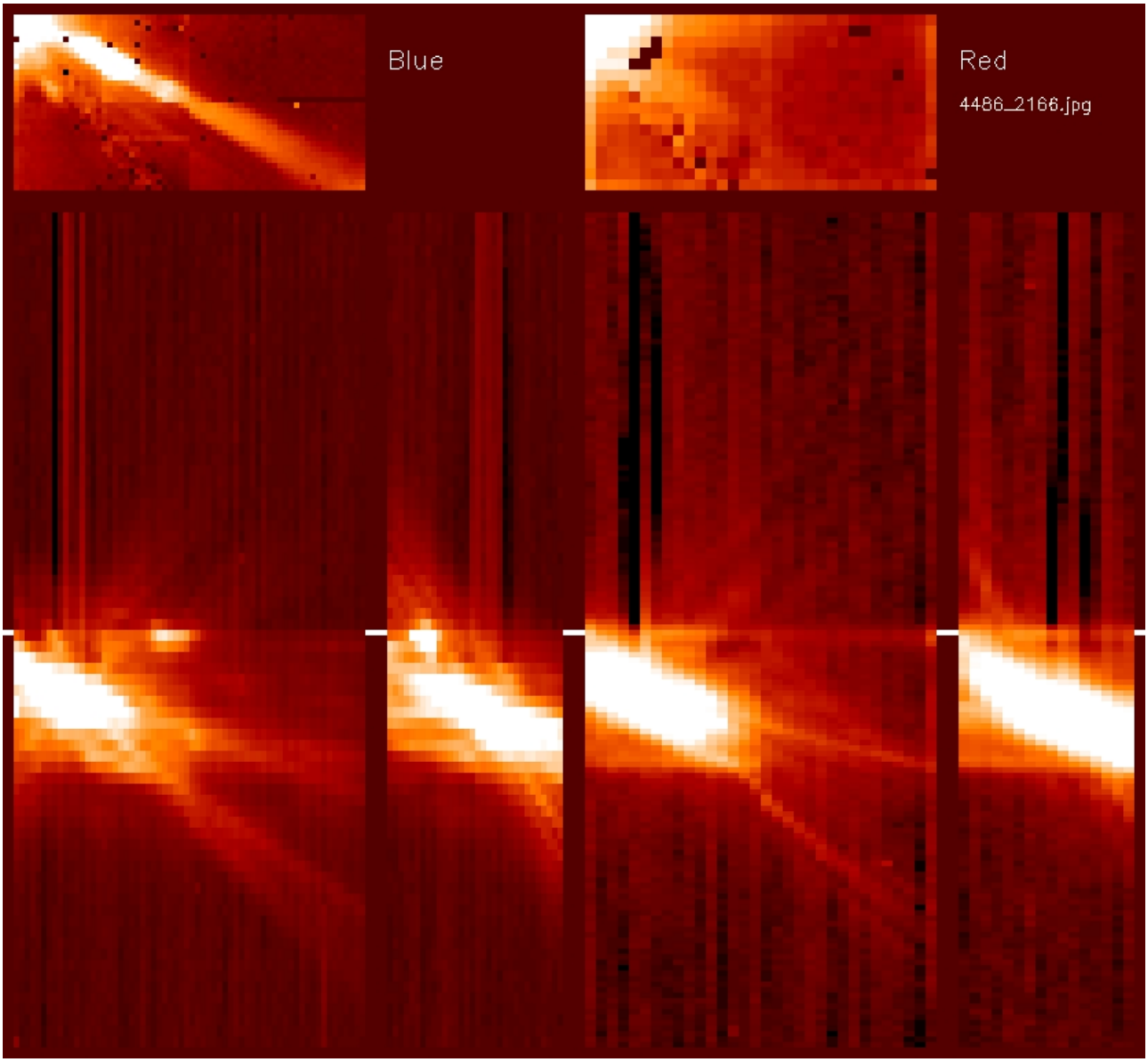

Figure 21: Diagonal streak in the blue array, with Mars just outside the top left corner. At the same time the signal in red array is generally elevated. The bottom panels show cuts through pixel 14,14 of the blue array and 7,7 of the red array, as a function of time rising upwards.

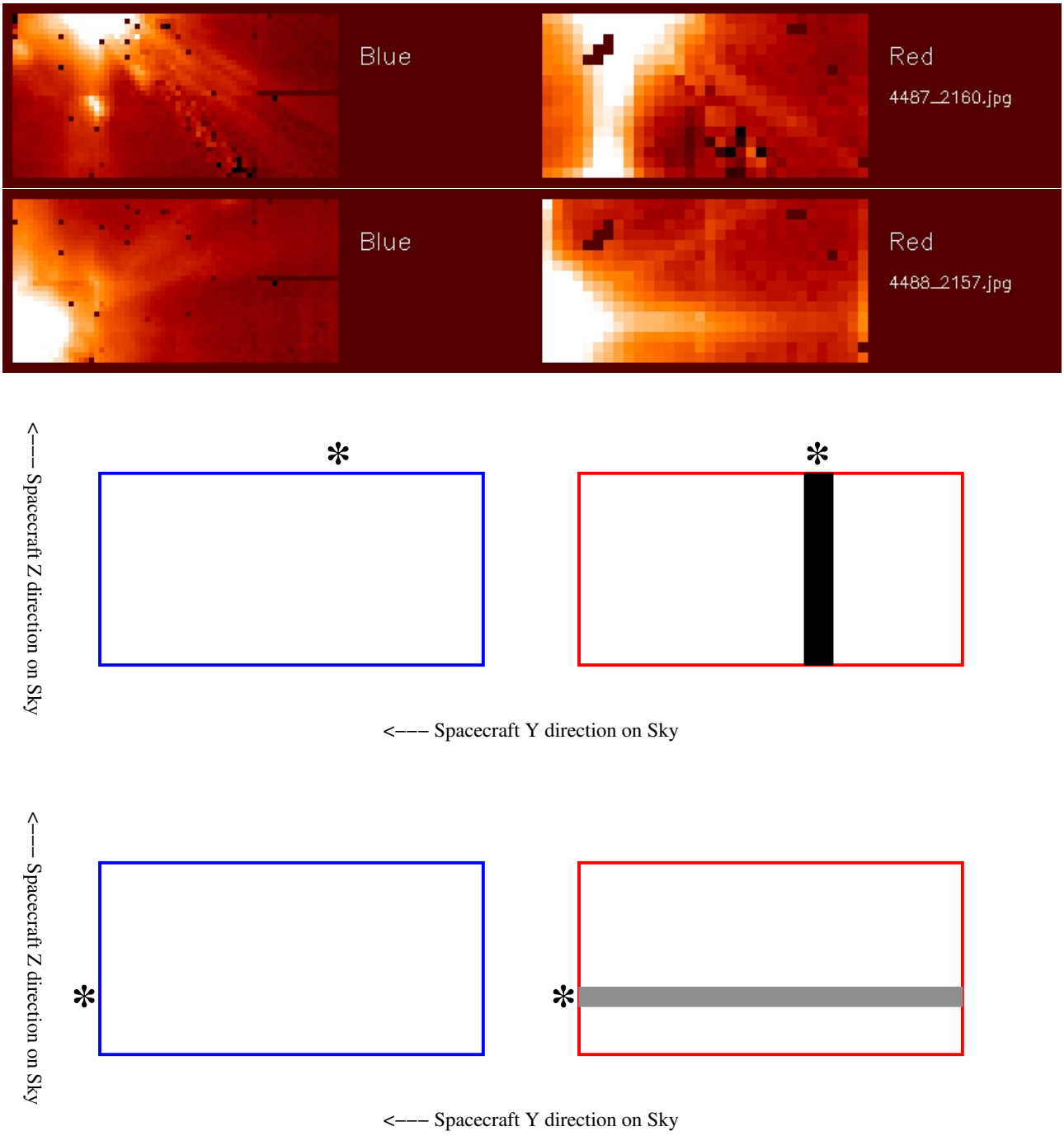

Figure 22: Red streaks. Top: vertical reflection with the source just off the upper array edge. Bottom: horizontal reflection with the source just off the left array edge.

individual most affected frame.

It is possible that these features contribute to the linear PSF feature in vertical (Z) direction (Sect 5.1) that aligns with one of the six diffraction spokes caused by the secondary support, but is too strong in comparison to the other spokes. The better sampled Mars mapping from OD906 may be used in the future to better test whether the phenomenon occurs along the full edges of the red array or just small parts. This mapping may also help verifying whether the shorter and more asymmetric linear feature seen in blue has a similar origin. This is plausible but not yet demonstrated from the data and analysis in hand.

6.6 Implications of peculiar effects

The reflections, ghosts, and crosstalk effects presented here are very faint relative to the source and will be irrelevant for most science cases. Their total effect on the encircled energy is implicitly captured in the encircled energy fraction (EEF) curves derived below.

They may however need explicit consideration for a subclass of observations which are trying to detect very faint sources or structures near very bright sources, with a dynamic range above $\sim 10^3$. Given that the effects strongly depend on the path of the source crossing the array, it may be advisable to supplement the source observations inside the program with an explicit PSF standard observation taken with *exactly* same AOR layout in array coordinates.

7 Effects of data reduction methods and of source SED

7.1 Effects of highpass filtering

If using the masking and highpassfiltering reduction scheme with small filtering radii to boost point source sensitivity, the wings of the PSF will be obviously reduced. Since details will depend on the adopted high pass filter parameters, masking strategy, and source properties, no quantitative results are provided here. A dedicated technical note is in preparation (P. Popesso et al. arXiv:1211.4257).

7.2 Standard data reduction vs. recentering

Band	Speed arcsec/sec	FWHM arcsec αTau OD118 normal processing	PA deg	FWHM arcsec αTau OD118 recentered	PA deg	Ratio
Blue	10	5.46×5.78		5.20×5.56		1.045
Blue	20	5.61×6.29		5.41×5.71		1.069
Blue	60	5.92×9.15	60.8	5.70×8.92	61.7	1.032
Green	10	6.67×6.95		6.52×6.75		1.026
Green	20	6.78×7.29		6.64×6.84		1.043
Green	60	7.01×9.89	61.6	6.84×9.64	61.8	1.025
Red	10	10.56×12.06	11.5	10.41×12.00	8.4	1.010
Red	20	10.86×12.18	16.5	10.57×12.05	9.7	1.010
Red	60	11.33×13.35	39.2	11.35×13.32	40.9	1.000

Table 7: Comparison of PSF widths for normal and recentered processing. Results are given from fitting 2-dimensional gaussians to the OD118 αTau PSFs. Ratio is the ratio of circularized PSF widths. *Array-to-map angle is 63deg for these observations.*

The recentering procedure, if applied, implicitly corrects for satellite pointing jitter, residual timing shifts satellite vs. instrument data, and inaccuracies of the spatial calibration, in particular the ArrayInstrument calfile. To give an example for the order of magnitude of the effect, we have reduced the same OD118 αTau data once with a normal script and then with recentering. Table 7 summarizes the results and the ratio of circularized PSF widths, Ratio $= \sqrt{\mathrm{FWHMa} \times \mathrm{FWHMb}_{\mathrm{Normal}}}/\sqrt{\mathrm{FWHMa} \times \mathrm{FWHMb}_{\mathrm{Recentered}}}$.

For these particular observations the increase of PSF width in normal processing is typically a few % but is expected to be a function of, e.g., pointing quality during a particular observation.

7.3 Effects of source SED

Because of the large spectral width of the PACS filters, noticeable effects of SED slope on the PSF width are expected. We verify this by dedicated observations of the Blazar 3C345 in comparison to the α Tau data. Both are fixed targets and observed with same AOR setup. No recentering was applied due to the faintness of 3C345, which also prevents analysis beyond the determination of PSF width (Fig. 24). Table 8 shows a PSF width that is on average lower by a few % for αTau compared to 3C345, with scatter due to the weakness of 3C345.

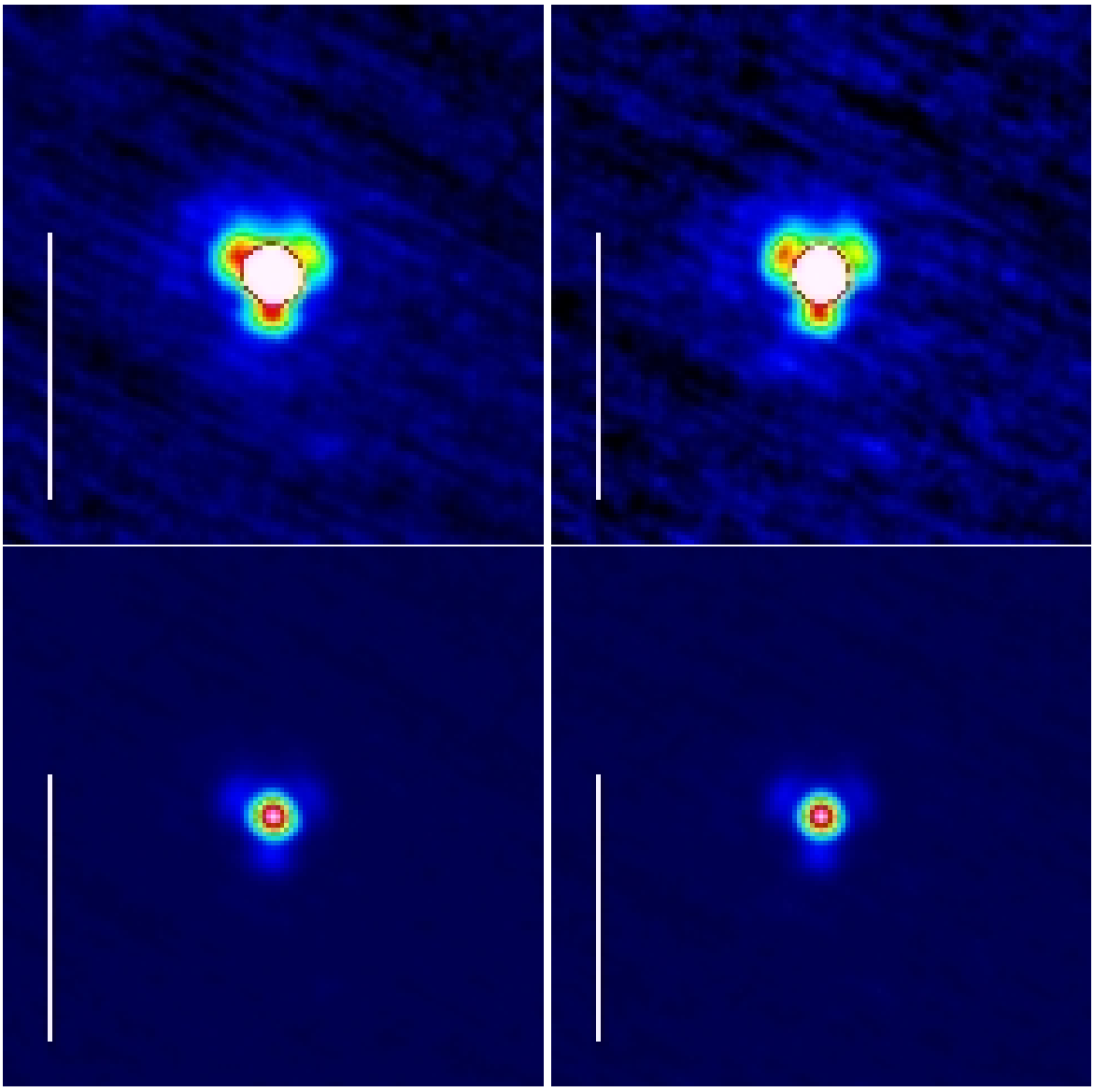

Figure 23: Slight sharpening effect of recentering on the PSF. The same green 20 arcsec/sec αTau observation is shown on the left with normal processing and on the right recentered. Top and bottom are different display cuts.

Band	Speed arcsec/sec	FWHM arcsec αTau OD118 normal processing	PA deg	FWHM arcsec 3C345 OD127 normal processing	PA deg	Ratio
Blue	10	5.46×5.78		5.73×5.86		0.969
Blue	20	5.61×6.29		5.85×6.01		1.002
Blue	60	5.92×9.15	60.8	5.62×10.82	66.3	0.944
Green	10	6.67×6.95		6.92×7.32		0.957
Green	20	6.78×7.29		6.83×7.46		0.985
Green	60	7.01×9.89	61.6	6.96×11.65	66.0	0.925
Red	10	10.56×12.06	11.5	10.89×12.42	13.8	0.970
Red	20	10.86×12.18	16.5	10.72×12.29	16.8	1.002
Red	60	11.33×13.35	39.2	12.13×15.40	49.0	0.900

Table 8: Comparison of PSF widths for αTau (blue Rayleigh-Jeans source) and 3C345 (red continuum). Ratio is the ratio of circularized PSF widths. *Array-to-map angle is 63deg for these observations.*

We can compare these results to expectations from the modelled 'as built' Herschel PSF of PICC-ME-TN-029, after convolution with the PACS pixel size for f_λ SED slope of -4 (roughly matching αTau) and -1 (roughly matching 3C345). We derive for the model PSFs circularized FWHM ratios of 0.979, 0.971, and 0.956 which are consistent with Table 8 given the S/N of the 3C345 data, and the presence of PSF effects that are not covered by the model.

7.4 Effects of drizzling and of map pixel size

Band	Speed arcsec/sec	FWHM arcsec Vesta OD160 pixfrac 1	PA deg	FWHM arcsec Vesta OD160 pixfrac 0.1	PA deg	Ratio
Blue	10	5.20×5.56		4.78×5.12		1.087
Green	10	6.54×6.78		6.24×6.48		1.047
Red	10	10.38×11.97	6.1	9.53×11.14	6.5	1.082

Table 9: Example of the effect of drizzling on the PSF width, comparing results of a Vesta recentered reduction with standard PhotProject (pixfrac 1) with a drizzled reduction with pixfrac 0.1.

By default, PACS maps created with the PhotProject tool assume in projection an active pixel size of 640μm within the pixel pitch of 750μm. This 'Okumura-Gastaud constant' is guided by the physical structure of the bolometer pixels and their inter-pixel walls. 'Drizzling' by projecting with the assumption of smaller PACS pixels can reduce the noise correlation between neighbouring map pixels and also sharpen the PSF. A pixfrac parameter has been introduced to that purpose into the photProject module. Pixfrac 1 corresponds to 640μm active size and smaller values to proportionally smaller linear sizes of the active area.

Figure 25 and Table 9 present an example showing that such drizzling can influence the PSF width at the 5% to 9% level, for the map pixel size 1arcsec adopted in this note for the PSF analysis. The effect is smallest in green where the PSF width is already better sampled by the natural PACS pixel size. Starting from v2.0, PSF images are released for both these cases pixfrac=1.0 and pixfrac=0.1.

In real PACS photometer reductions, users may choose not only different values for the pixfrac parameter but also different sizes of pixels in the resulting map, via the pixsize parameter in photProject. In Tables 10 to 12 we

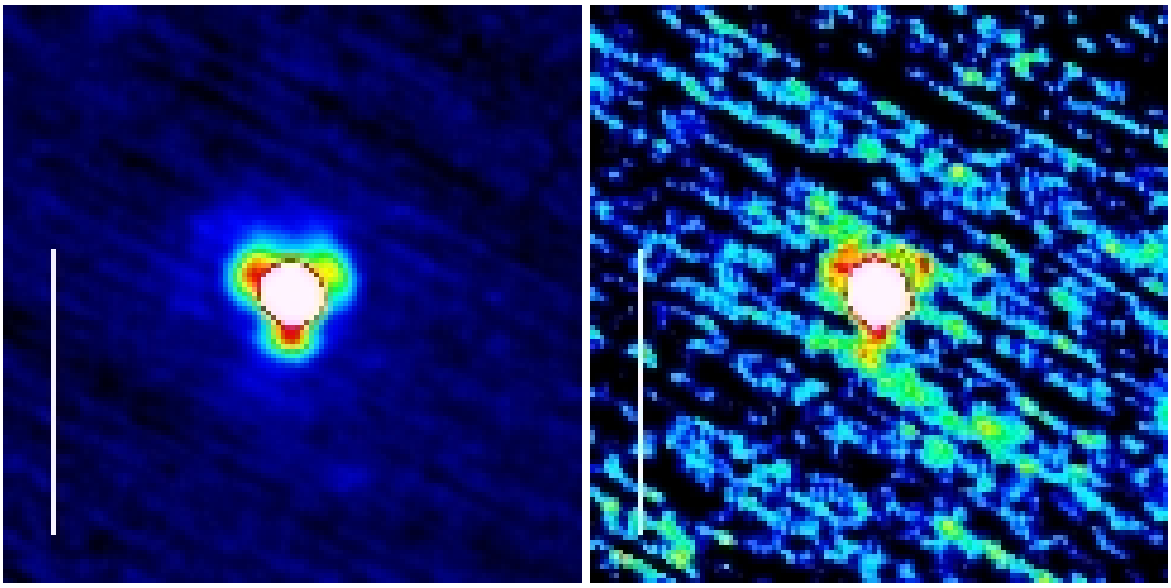

Figure 24: Example of observation to verify the effect of SED slope on PSF width. Left is a green 20/arcsec/sec αTau with normal processing, right the equivalent observation for 3C345. Given flux and S/N of 3C345, comparison is limited to PSF width confirming the expected increase for a red source.

present as an example the ensuing circularized FHWM of the PSF for blue, green, and red Vesta observations. These use medium speed 20 arcsec/sec data from OD345, and a reduction without recentering. The pixfrac and pixsize parameters are varied over a range that may be chosen in real reductions. Again, effects are least noticeable in the intrinsically better sampled green channel.

Pixfrac Pixsize	0.01	0.10	0.20	0.50	1.00
1.00	5.438	5.443	5.458	5.547	5.866
1.20	5.459	5.469	5.482	5.571	5.890
1.40	5.497	5.497	5.512	5.602	5.919
1.60	5.528	5.536	5.548	5.636	5.952
1.80	5.583	5.581	5.591	5.675	5.989
2.00	5.617	5.623	5.636	5.721	6.031
2.50	5.745	5.750	5.764	5.849	6.154
3.00	5.869	5.871	5.884	5.968	6.271
3.20	5.908	5.913	5.927	6.008	6.309

Table 10: Circularized FWHM (arcsec) from a 2D Gaussian fit to the **blue** PACS PSF, for a range of pixsize (map pixel size in arcsec) and pixfrac (drizzling) parameters in photProject. Data are from Vesta OD345 Obsid 1342195472 (speed 20arcsec/sec, array-to-map angle +42), reduction without recentering.

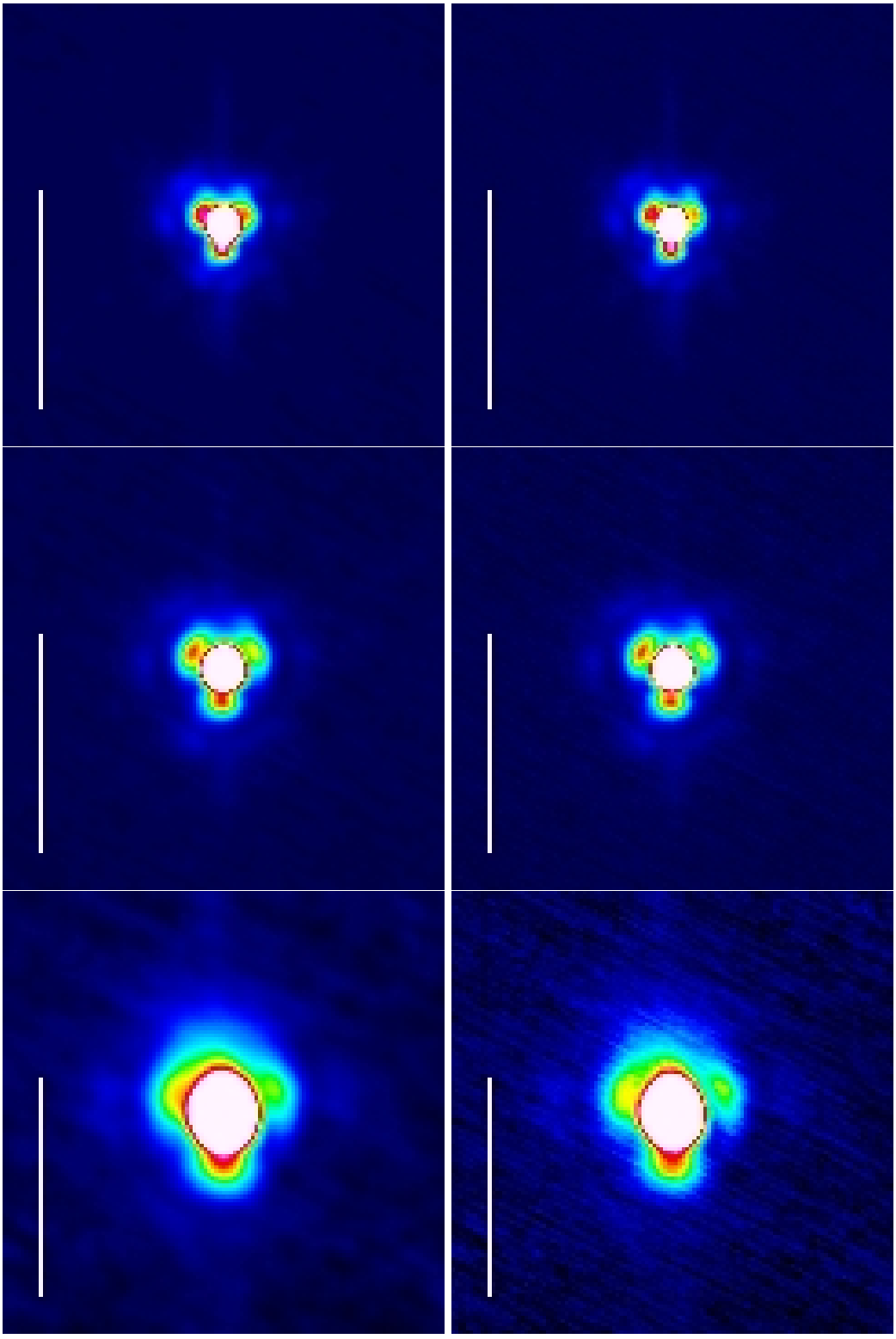

Figure 25: Sharpening effect of drizzling on the PSF for the same Vesta 10arcsec/sec observations, blue–green–red from top to bottom. Left: recentered, standard PhotProject (pixfrac 1). Right: recentered, drizzled with pixfrac 0.1.

Pixfrac Pixsize	0.01	0.10	0.20	0.50	1.00
1.00	6.628	6.631	6.641	6.703	6.932
1.20	6.644	6.646	6.656	6.721	6.950
1.40	6.677	6.680	6.687	6.744	6.969
1.60	6.697	6.696	6.706	6.768	6.995
1.80	6.723	6.727	6.733	6.795	7.023
2.00	6.751	6.755	6.763	6.826	7.055
2.50	6.844	6.850	6.860	6.922	7.147
3.00	6.968	6.970	6.977	7.038	7.264
3.20	7.015	7.024	7.033	7.093	7.317

Table 11: Circularized FWHM (arcsec) from a 2D Gaussian fit to the **green** PACS PSF, for a range of pixsize (map pixel size in arcsec) and pixfrac (drizzling) parameters in photProject. Data are from Vesta OD345 Obsid 1342195476 (speed 20arcsec/sec, array-to-map angle +42), reduction without recentering.

Pixfrac Pixsize	0.01	0.10	0.20	0.50	1.00
1.00	10.455	10.465	10.491	10.667	11.308
1.50	10.489	10.499	10.525	10.699	11.339
2.00	10.540	10.544	10.568	10.745	11.384
2.50	10.603	10.604	10.629	10.805	11.441
3.00	10.662	10.671	10.702	10.876	11.510
3.50	10.747	10.757	10.784	10.958	11.592
4.00	10.838	10.843	10.873	11.054	11.691
5.00	11.100	11.110	11.134	11.306	11.924
6.00	11.359	11.373	11.402	11.570	12.174
6.40	11.469	11.471	11.496	11.661	12.264

Table 12: Circularized FWHM (arcsec) from a 2D Gaussian fit to the **red** PACS PSF, for a range of pixsize (map pixel size in arcsec) and pixfrac (drizzling) parameters in photProject. Data are from Vesta OD345 Obsid 1342195472 (speed 20arcsec/sec, array-to-map angle +42), reduction without recentering.

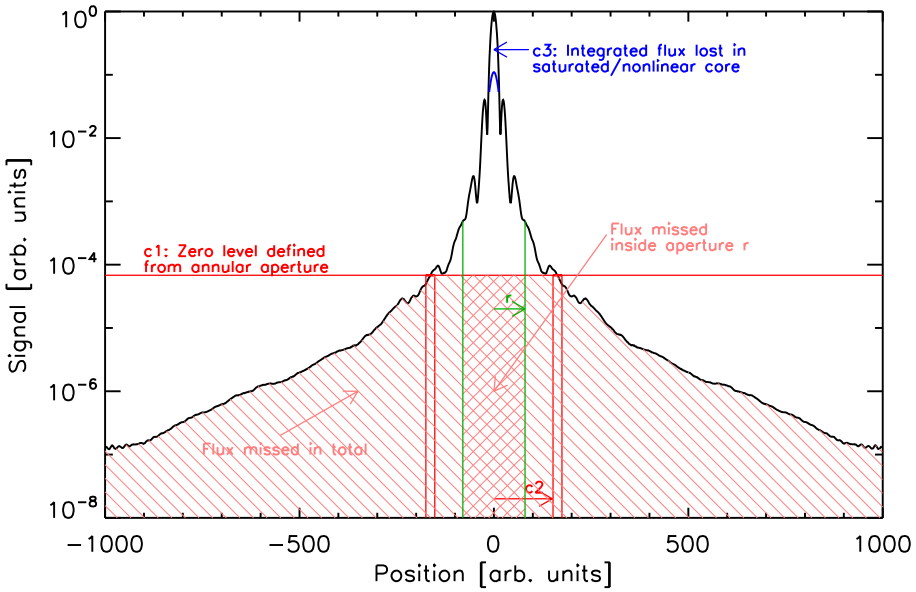

Figure 26: Schematic repesentation of effects on the measured encircled energy fraction. The ideal EEF would divide the integral of the true PSF (black) inside an aperture r (green) by the integral to infinity. For the 'observed' EEF the background subtraction, setting to 0 the flux in an annulus outside radius c2, will cause flux to be missed both within the aperture and from the total which in addition is cut at radius c2. Additionally flux c3 may be lost in the PSF core due to nonlinearity or saturation.

8 Encircled energy diagrams

'Encircled energy fractions' (EEFs) for various aperture sizes are a key quantity in homogenizing point source photometry obtained with different methods or aperture sizes, and in establishing the extended source calibration of PACS. Practical limitations in its determination arise from S/N, limited dynamical range and saturation, and from the reduction methods described above. This is qualitatively illustrated in Fig. 26.

We adopt the definition

$$EEF(r) = \frac{\int_0^r \int_0^{2\pi} PSF(r,\phi) d\phi dr}{\int_0^\infty \int_0^{2\pi} PSF(r,\phi) d\phi dr}$$

but note that several factors limit evaluation of the total integral to a sufficient ∼percent accuracy. (1) Observations of bright but clearly unsaturated sources like Vesta run out of S/N at large radii. (2) The scheme of subtracting background in an annular aperture reduces the PSF at all radii by the average value within that annulus. Note that skipping this step would simply replace it with a less well defined equivalent subtraction, due to the masked highpass filtering. (3) For the brightest sources like Mars, signal will be missing in the PSF core due to nonlinearity and/or saturation. Fig. 26 gives a cartoon representation of these factors.

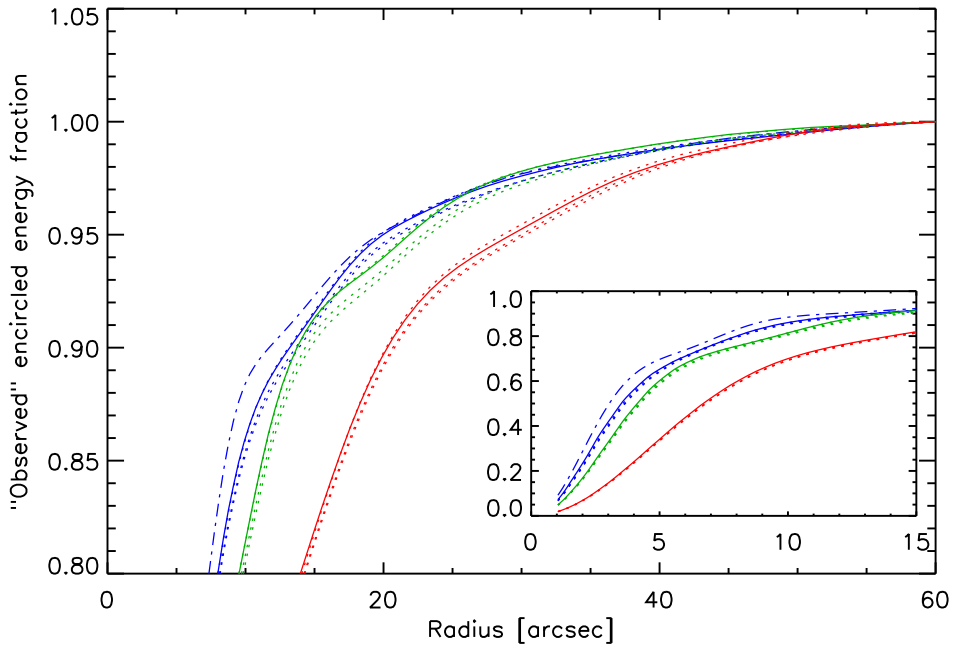

Figure 27: 'Observed' encircled energy fraction as a function of circular aperture radius for the three bands. Derived from slow scan (continuous line) and medium speed scan (dashed lines) OD160 and OD345 Vesta data. The EEF fraction shown is normalized to the signal in aperture radius 60arcsec, with background subtraction done in an annulus between radius 61 and 70 arcsec. For blue only, we add with a dot-dashed line the model expectation.

Effectively we are thus using the HIPE annularSkyAperturePhotometry function to obtain from an observation an 'observed' EEF that is related to the true PSF like

$$EEF_{obs}(r) = \frac{\int_0^r \int_0^{2\pi} (PSF(r,\phi) - c1) d\phi dr - c3}{\int_0^{c2} \int_0^{2\pi} (PSF(r,\phi) - c1) d\phi dr - c3}$$

where c1 is the average of the true PSF in the annulus used for sky subtraction, c2 the radius of the aperture to which the 'total' PSF was actually integrated, and c3 the flux missing in the PSF core due to saturation/nonlinearity, assuming that both r and c2 reach beyond this core. Note that the total PSF integral is too low not only via c1 and potentially c3 but also by lacking the outer PSF part $\int_{c2}^{\infty} \int_0^{2\pi} PSF(r,\phi) d\phi dr$.

8.1 Ancillary information

We are first presenting raw 'observed' EEFs of this type, from both observations and modelling, before attempting to estimate the true EEF.

The PSFs derived from the OD160 and OD345 Vesta data are of sufficient S/N to derive observed encircled energy fractions for the 3 bands as a function of the radius of a circular aperture (Fig. 27). The EEF fraction

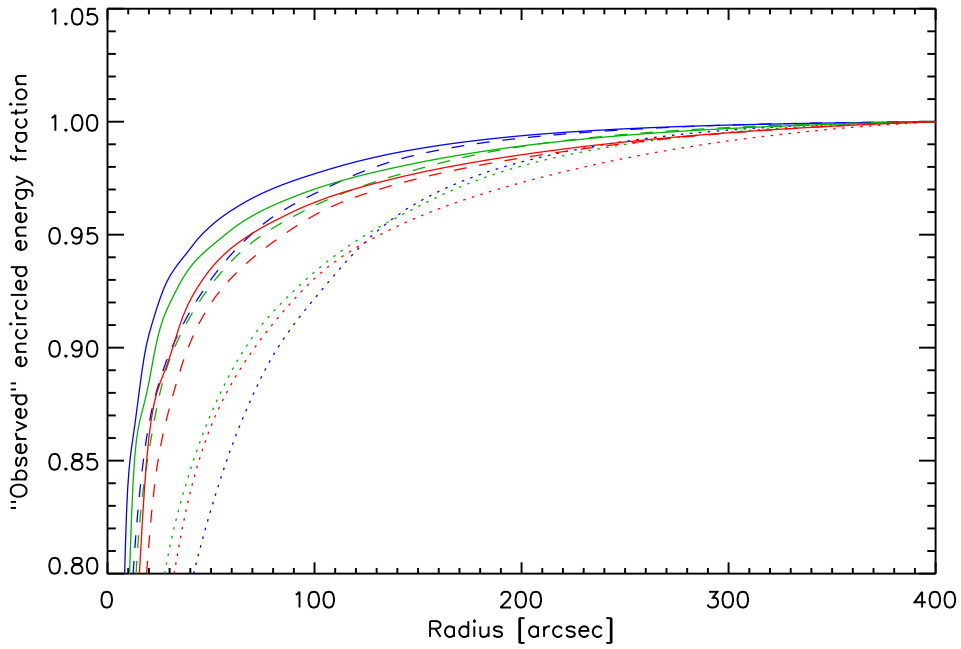

Figure 28: 'Observed' encircled energy fraction as a function of circular aperture radius for the blue, green, and red models (continuous), the Mars OD888 data (dotted) uncorrected for saturation, and the Mars OD888 data corrected for saturation (dashed). The observed PSF has more energy at large radii than the model.

shown is normalized to the signal in aperture radius c2=60arcsec, with background subtraction done in an annulus between radius 61 and 70 arcsec. The agreement between the four measurements at two different scanspeeds is very satisfactory at these large radii, supporting the quality of the data. We later average them for deriving fiducial results.

A radius c2 of 60arcsec will miss a nonnegligible part of the PACS PSF. Both modelled PSFs (PICC-ME-TN-029) or large field observations of a super-bright source like Mars could be used to determine this missing flux. The Mars observations could in principle be of limited use if dominated by saturation aftereffects, the combined OD888 mars maps (see above) bypass this issue completely.

Figure 28 compares the EEF from the model PSFs to the EEF from the Mars result, first uncorrected and then corrected for the Mars flux c3 lost due to saturation. Both are consistently processed to an observed EEF out to c2=400arcsec. It appears that the real PSF has more energy at radii above 60arcsec, but only at an excess level ∼2–3% above the model. This excess likely relates to the different anomalous and ghost effects in PACS that were discussed above, which are not included in the model PSF. As a consequence, extrapolation of the Vesta PSFs to larger radii should be done with observed data rather than with telescope PSF models.

8.2 Derivation of EEF curves

Based on these considerations, we derive EEF curves out to 1000 arcsec from the combination of Vesta and Mars data. In this process, the main steps and assumptions are:

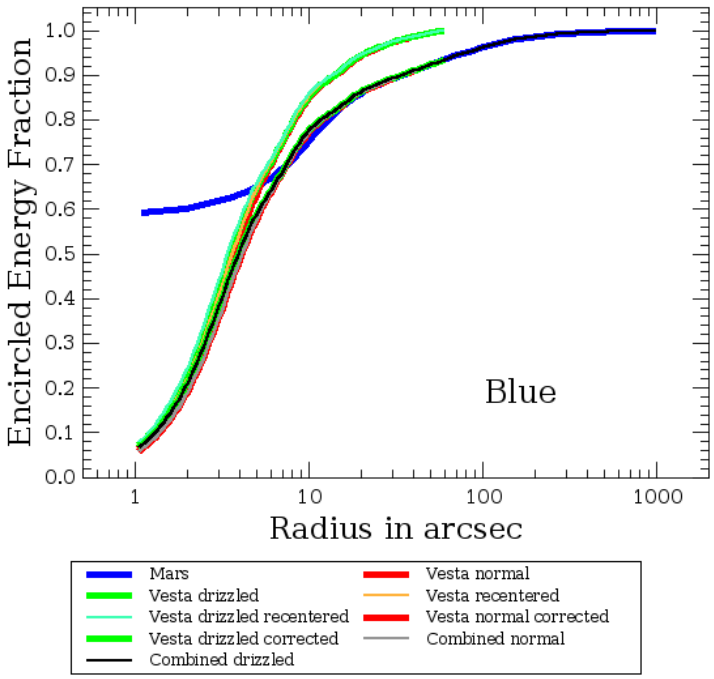

Figure 29: Encircled Energy Fraction for blue. Contributing Mars and Vesta data are shown along with the final combination.

- Mars EEF curves for all three PACS bands are derived out to c2=1000arcsec where the OD888 Mars maps run out of visible signal. Any flux outside this radius is ignored. The central region of these EEF curves is affected by flux lost due to saturation (c3), and smeared due to the nonnegligible angular diameter of Mars during the observation (about 6arcsec).
- The flux c3 lost in the central region of the Mars map can be determined comparing the map integral to the nominal Mars flux at the time of observation (Table 3). The EEF curve is corrected, placing this flux nominally at r=0. The resulting EEF is still incorrect at small radii.
- For each band, all Vesta PSFs from OD160 and and OD345 taken with scanspeed 10 (low) or 20 arcsec/sec (medium) are averaged and 'observed' EEF curves out to c2=60arcsec derived. For the versions to be distributed, no recentering was applied, to be representative for a typical reduction. Versions without drizzling and for drizzling with pixfrac 0.1 were derived.
- From the Mars EEF, the constants c1 applicable to the Vesta maps are derived.
- The Vesta EEF is corrected for the flux lost due to the nonzero c1 and the flux outside radius c2.
- The two corrected EEFs are overplotted. The factor for the flux lost in the Vesta processing is iterated until the EEF curves visually match at radii approaching 60arcsec. Deviations at smaller radii are expected due to the saturation/smearing effects on the Mars data.

Figs. 29 to 31 show the resulting encircled energy fraction curves out to 1000 arcsec, separately for each band and including the contributing Mars and Vesta data. Fig. 32 displays the final combinations for all three bands. We note that the flux in the combined encircled energy curves outside r=60 arcsec is 6.4%, 7.1%, and 8.6% in blue, green, and red. In the Vesta processing, the fraction of flux missing combining this loss at large radii with the oversubtraction in the inner region is 8.9% (blue) 9.4% (green) and 10.9% (red). Recall that the effect of

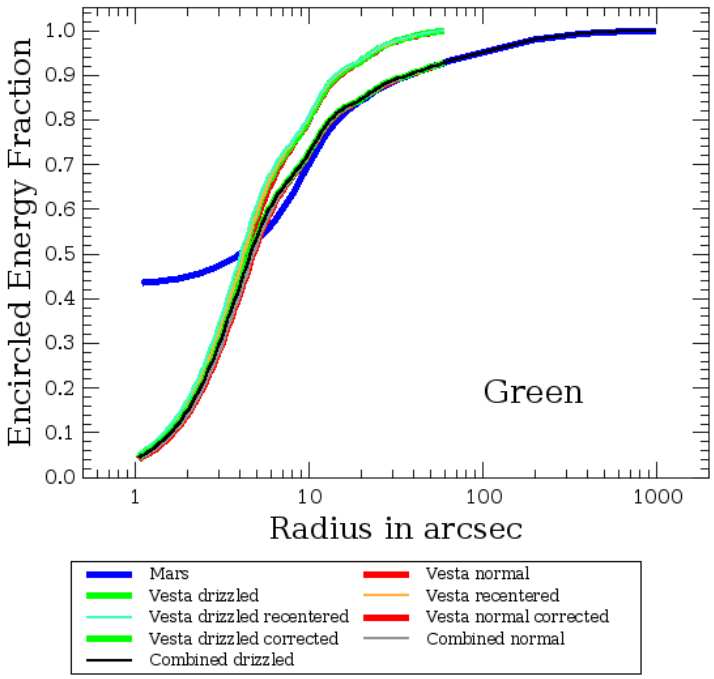

Figure 30: Encircled Energy Fraction for green. Contributing Mars and Vesta data are shown along with the final combination.

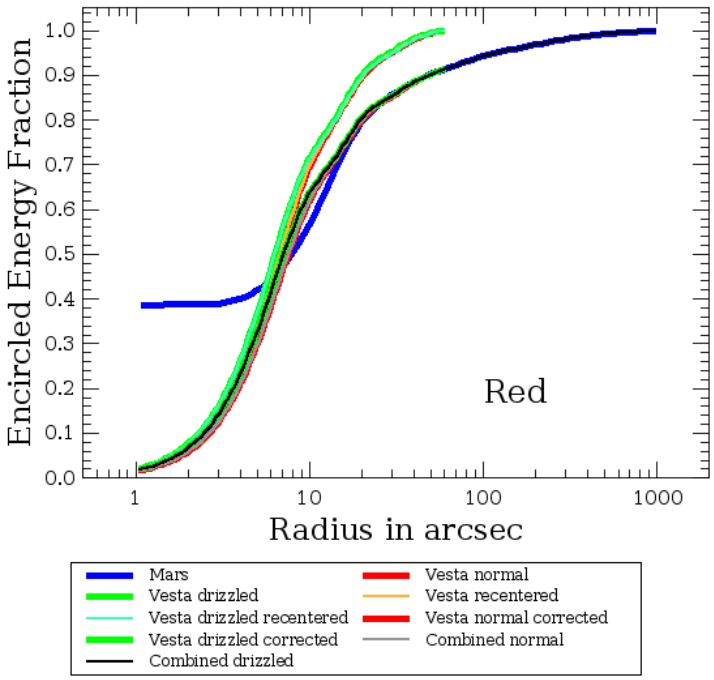

Figure 31: Encircled Energy Fraction for red. Contributing Mars and Vesta data are shown along with the final combination.

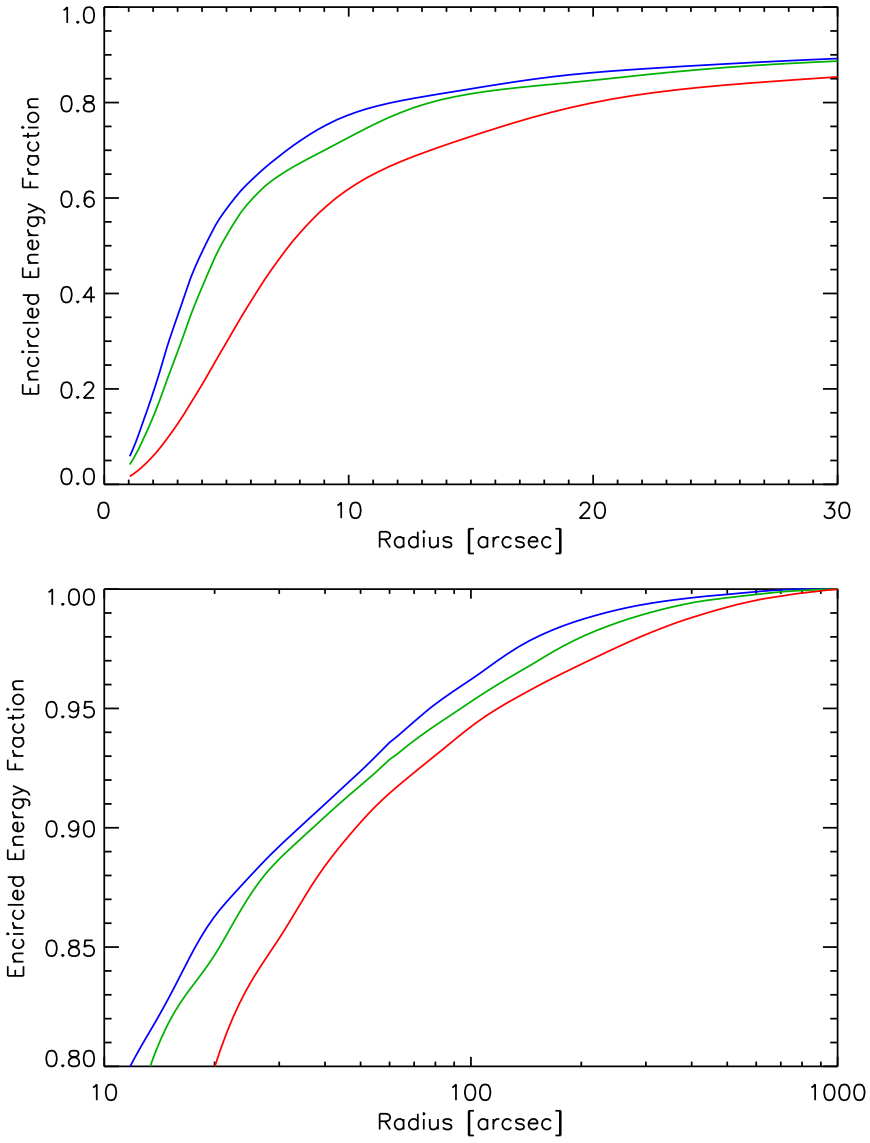

Figure 32: Combined Encircled Energy Fractions for all three PACS bands, as applicable to medium speed and slow speed prime mode data.

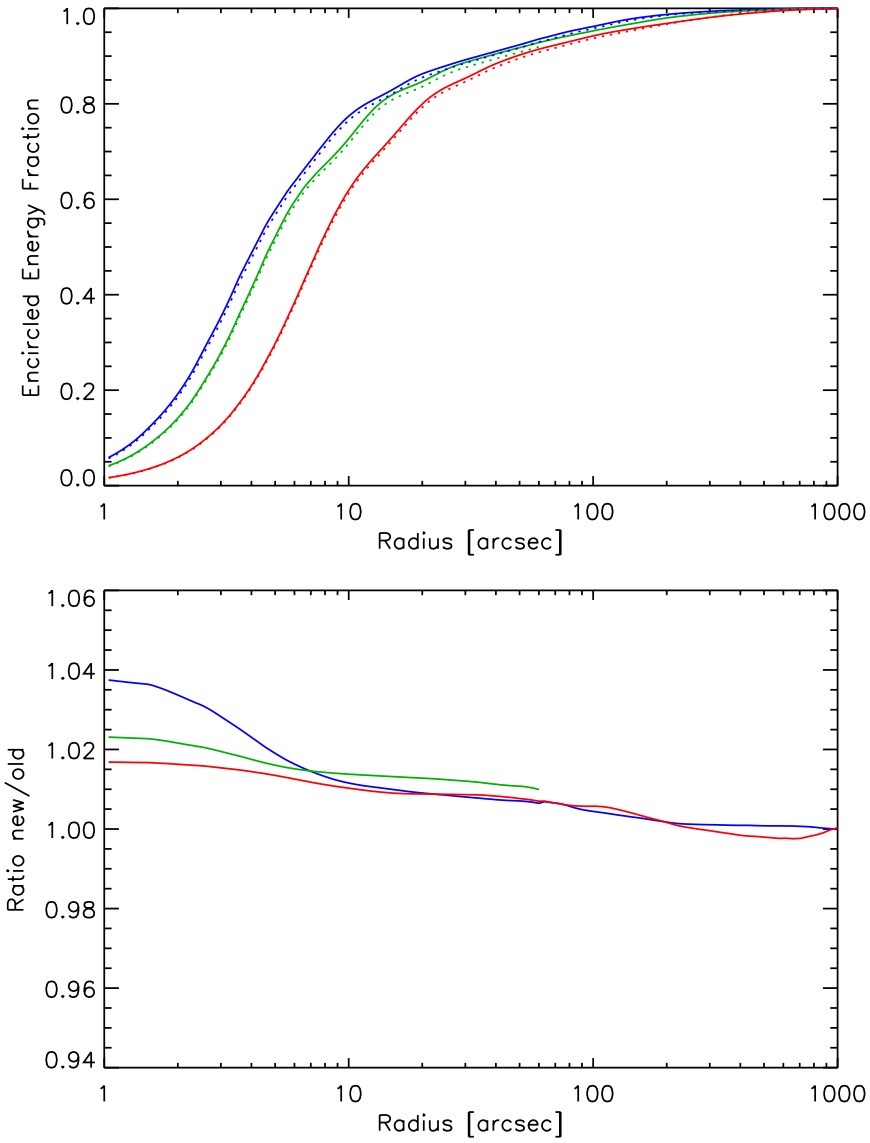

Figure 33: Comparison of the v2.0 Encircled Energy Fractions released with this note (new) and version 1.0 (old).

ghosts and other peculiar effects at large radii, estimated above to be a few %, will vary with detailed AOR layout and source crossing path. For example, the Mars OD137 maps have slightly larger flux at few arcmin radius than the OD888 maps.

The comparison of the new version 2.0 EEFs with the older v1.0 shows only minor differences (Fig. 33).

8.3 Encircled energy fraction for SPIRE/PACS parallel mode and PACS prime mode fast scan

Scan speed and additional data averaging in the blue camera lead to a considerable broadening of the parallel mode PSF for 60arcsec/sec in blue and green, and minor broadening for 60 arcsec/sec red and 20 arcsec/sec blue and green – see Sect. 5.2 for details. Dedicated parallel mode EEFs were hence derived for v2.1 of this note, using the OD345 'fake parallel mode' Vesta data in conjunction with Mars OD888, and methods as described above.

Fig. 34 shows a comparison of the corresponding EEF curves, and a zoom-in. The additional parallel mode EEF curves are provided in the tarball associated to this note. At 20arcsec/sec parallel mode and prime EEF are rather close even in blue and green. There are considerable differences between 60arcsec/sec parallel and 20arcsec/sec prime, in particular for blue and green.

A small set of observations in the Herschel archive uses the 60arcsec/sec PACS prime mode. Dedicated EEFs for this case and the blue and green filters are provided since v2.2. For red, the instrument setting and PSF are identical in prime and parallel, the EEF for the common fast mode parallel observations is hence applicable also for the rare prime mode fast scans in the red band.

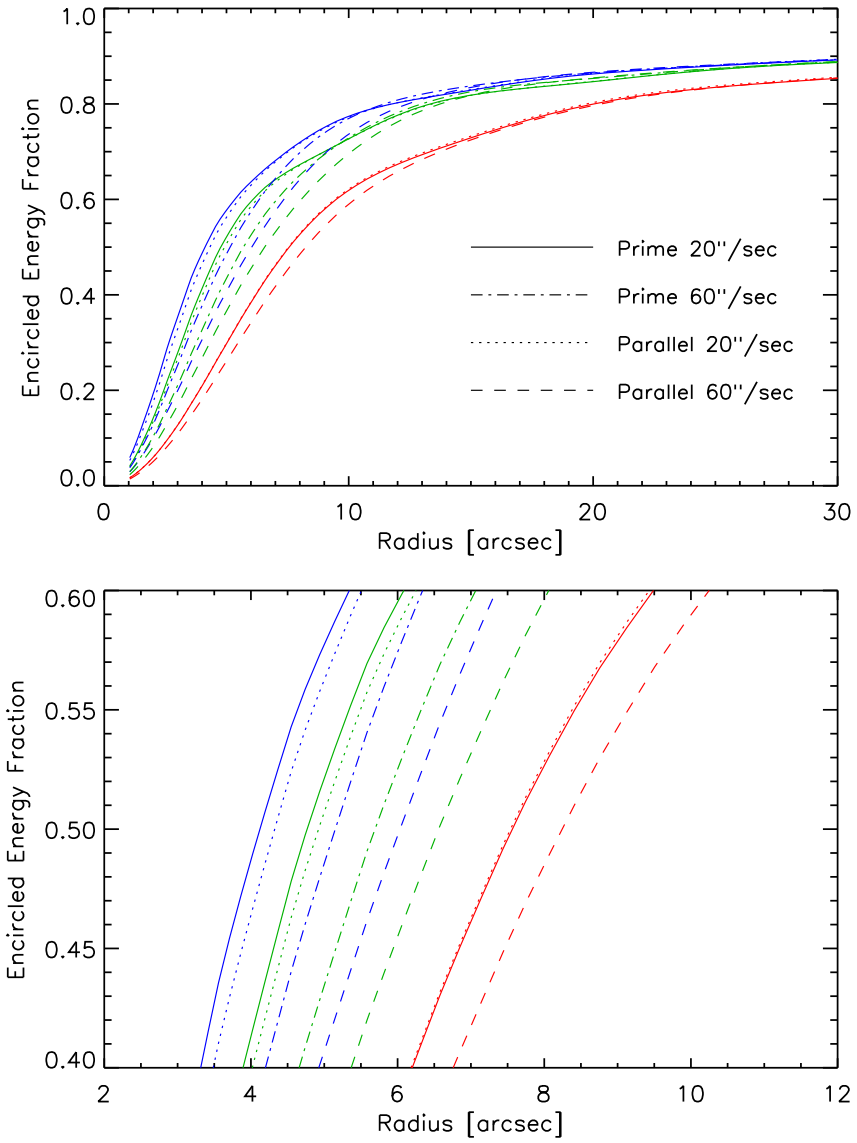

Figure 34: Combined Encircled Energy Fractions for all three PACS bands. EEFs for the two SPIRE/PACS parallel mode scanspeeds are shown in comparison to the default prime 20arcsec/sec. The parallel mode EEFs apply to the equal weight of the scan and crossscan at array-to-map angle ±42 degrees. The rare case of prime 60arcsec/sec is also shown for blue and green. For red, this is identical to parallel mode 60arcsec/sec.

9 Data products accompanying this note

Tarball PACSPSF_PICC-ME-TN-033_v2.2.tar.gz contains the following data:

- Vesta PSFs from OD160 and OD345 data. All are processed with a masking radius 60 arcsec and explicitly subtracting the background at r=61-70arcsec. Total signal inside r=60arcsec is normalized. File names follow a scheme psf20_band_speed_source_OD_ama_remarks.fits e.g. psf20_red_20_vesta_od345_ama+42_recentered.fits, where OD is the operational day the data were taken and ama the scan direction as given by the 'array-to-map angle' in degrees (see Appendix). Each psf file comes in four flavours for the four combinations of not recentered vs. recentered and pixfrac=1. vs. pixfrac=0.1. 'Recentered' images are labeled as such, '0p10' refers to pixfrac=0.1. For blue and green there is a 1:1 correspondence to OBSIDs in the observation summary table above, while the red data average data from equivalent blue+red and green+red OBSIDs. Note that the Vesta observations from these ODs are publicly available from the Herschel Science Archive for experiments on the effect of other reduction schemes or parameters.
- Blue, green and red EEF curves from the combination of Vesta and Mars data. Columns in the files EEF_blu_20.txt etc. are (1) Radius in arcsec (2) Encircled fraction of the energy out to r=1000 arcsec for pixfrac 1 (3) Encircled fraction of the energy out to r=1000 arcsec for pixfrac 0.1 (4) Uncorrected Vesta EEF out to r=60 arcsec for pixfrac 1 (5) Uncorrected Vesta EEF out to r=60 arcsec for pixfrac 0.1.
- Blue, green and red EEF curves EEF_blu_60para_21.txt etc. for parallel mode, from the combination of Vesta and Mars data. Curves are provided for both 60arcsec/sec and 20 arcsec/sec.
- Blue and green EEF curves EEF_blue_60_22.txt etc. for prime mode fast scan, from the combination of Vesta and Mars data. For red in this prime/fast mode the parallel mode EEF_red_60para_21.txt shall be used since the PSF is the same.

Note that the v2.1 tarball is identical to the v2.0 one, with the exception of the additional parallel mode EEF curves. The v2.2 further added EEF in blue and green for the rare 60arcsec/sec prime mode, again it is identical otherwise.

The individual files in PACSPSF_PICC-ME-TN-033_v2.2.tar.gz are:

```
EEF_blu_20.txt
EEF_grn_20.txt
EEF_red_20.txt
EEF_blu_60para_21.txt
EEF_grn_60para_21.txt
EEF_red_60para_21.txt
EEF_blu_20para_21.txt
EEF_grn_20para_21.txt
EEF_red_20para_21.txt
EEF_blu_60_22.txt
EEF_grn_60_22.txt
psf20_blu_10_vesta_od160_ama+63_0p10.fits
psf20_blu_10_vesta_od160_ama+63_0p10recentered.fits
psf20_blu_10_vesta_od160_ama+63.fits
psf20_blu_10_vesta_od160_ama+63_recentered.fits
psf20_blu_20para_vesta_od160_ama+63_0p10.fits
```

psf20_blu_20para_vesta_od160_ama+63_0p10recentered.fits
psf20_blu_20para_vesta_od160_ama+63.fits
psf20_blu_20para_vesta_od160_ama+63_recentered.fits
psf20_blu_20para_vesta_od345_ama-42_0p10.fits
psf20_blu_20para_vesta_od345_ama+42_0p10.fits
psf20_blu_20para_vesta_od345_ama-42_0p10recentered.fits
psf20_blu_20para_vesta_od345_ama+42_0p10recentered.fits
psf20_blu_20para_vesta_od345_ama-42.fits
psf20_blu_20para_vesta_od345_ama+42.fits
psf20_blu_20para_vesta_od345_ama-42_recentered.fits
psf20_blu_20para_vesta_od345_ama+42_recentered.fits
psf20_blu_20_vesta_od160_ama+63_0p10.fits
psf20_blu_20_vesta_od160_ama+63_0p10recentered.fits
psf20_blu_20_vesta_od160_ama+63.fits
psf20_blu_20_vesta_od160_ama+63_recentered.fits
psf20_blu_20_vesta_od345_ama-42_0p10.fits
psf20_blu_20_vesta_od345_ama+42_0p10.fits
psf20_blu_20_vesta_od345_ama-42_0p10recentered.fits
psf20_blu_20_vesta_od345_ama+42_0p10recentered.fits
psf20_blu_20_vesta_od345_ama-42.fits
psf20_blu_20_vesta_od345_ama+42.fits
psf20_blu_20_vesta_od345_ama-42_recentered.fits
psf20_blu_20_vesta_od345_ama+42_recentered.fits
psf20_blu_60para_vesta_od160_ama+63_0p10.fits
psf20_blu_60para_vesta_od160_ama+63_0p10recentered.fits
psf20_blu_60para_vesta_od160_ama+63.fits
psf20_blu_60para_vesta_od160_ama+63_recentered.fits
psf20_blu_60para_vesta_od345_ama-42_0p10.fits
psf20_blu_60para_vesta_od345_ama+42_0p10.fits
psf20_blu_60para_vesta_od345_ama-42_0p10recentered.fits
psf20_blu_60para_vesta_od345_ama+42_0p10recentered.fits
psf20_blu_60para_vesta_od345_ama-42.fits
psf20_blu_60para_vesta_od345_ama+42.fits
psf20_blu_60para_vesta_od345_ama-42_recentered.fits
psf20_blu_60para_vesta_od345_ama+42_recentered.fits
psf20_blu_60_vesta_od160_ama+63_0p10.fits
psf20_blu_60_vesta_od160_ama+63_0p10recentered.fits
psf20_blu_60_vesta_od160_ama+63.fits
psf20_blu_60_vesta_od160_ama+63_recentered.fits
psf20_blu_60_vesta_od345_ama-42_0p10.fits
psf20_blu_60_vesta_od345_ama+42_0p10.fits
psf20_blu_60_vesta_od345_ama-42_0p10recentered.fits
psf20_blu_60_vesta_od345_ama+42_0p10recentered.fits
psf20_blu_60_vesta_od345_ama-42.fits
psf20_blu_60_vesta_od345_ama+42.fits
psf20_blu_60_vesta_od345_ama-42_recentered.fits
psf20_blu_60_vesta_od345_ama+42_recentered.fits
psf20_grn_10_vesta_od160_ama+63_0p10.fits
psf20_grn_10_vesta_od160_ama+63_0p10recentered.fits
psf20_grn_10_vesta_od160_ama+63.fits
psf20_grn_10_vesta_od160_ama+63_recentered.fits
psf20_grn_20para_vesta_od160_ama+63_0p10.fits
psf20_grn_20para_vesta_od160_ama+63_0p10recentered.fits
psf20_grn_20para_vesta_od160_ama+63.fits

psf20_grn_20para_vesta_od160_ama+63_recentered.fits
psf20_grn_20para_vesta_od345_ama-42_0p10.fits
psf20_grn_20para_vesta_od345_ama+42_0p10.fits
psf20_grn_20para_vesta_od345_ama-42_0p10recentered.fits
psf20_grn_20para_vesta_od345_ama+42_0p10recentered.fits
psf20_grn_20para_vesta_od345_ama-42.fits
psf20_grn_20para_vesta_od345_ama+42.fits
psf20_grn_20para_vesta_od345_ama-42_recentered.fits
psf20_grn_20para_vesta_od345_ama+42_recentered.fits
psf20_grn_20_vesta_od160_ama+63_0p10.fits
psf20_grn_20_vesta_od160_ama+63_0p10recentered.fits
psf20_grn_20_vesta_od160_ama+63.fits
psf20_grn_20_vesta_od160_ama+63_recentered.fits
psf20_grn_20_vesta_od345_ama-42_0p10.fits
psf20_grn_20_vesta_od345_ama+42_0p10.fits
psf20_grn_20_vesta_od345_ama-42_0p10recentered.fits
psf20_grn_20_vesta_od345_ama+42_0p10recentered.fits
psf20_grn_20_vesta_od345_ama-42.fits
psf20_grn_20_vesta_od345_ama+42.fits
psf20_grn_20_vesta_od345_ama-42_recentered.fits
psf20_grn_20_vesta_od345_ama+42_recentered.fits
psf20_grn_60para_vesta_od160_ama+63_0p10.fits
psf20_grn_60para_vesta_od160_ama+63_0p10recentered.fits
psf20_grn_60para_vesta_od160_ama+63.fits
psf20_grn_60para_vesta_od160_ama+63_recentered.fits
psf20_grn_60para_vesta_od345_ama-42_0p10.fits
psf20_grn_60para_vesta_od345_ama+42_0p10.fits
psf20_grn_60para_vesta_od345_ama-42_0p10recentered.fits
psf20_grn_60para_vesta_od345_ama+42_0p10recentered.fits
psf20_grn_60para_vesta_od345_ama-42.fits
psf20_grn_60para_vesta_od345_ama+42.fits
psf20_grn_60para_vesta_od345_ama-42_recentered.fits
psf20_grn_60para_vesta_od345_ama+42_recentered.fits
psf20_grn_60_vesta_od160_ama+63_0p10.fits
psf20_grn_60_vesta_od160_ama+63_0p10recentered.fits
psf20_grn_60_vesta_od160_ama+63.fits
psf20_grn_60_vesta_od160_ama+63_recentered.fits
psf20_grn_60_vesta_od345_ama-42_0p10.fits
psf20_grn_60_vesta_od345_ama+42_0p10.fits
psf20_grn_60_vesta_od345_ama-42_0p10recentered.fits
psf20_grn_60_vesta_od345_ama+42_0p10recentered.fits
psf20_grn_60_vesta_od345_ama-42.fits
psf20_grn_60_vesta_od345_ama+42.fits
psf20_grn_60_vesta_od345_ama-42_recentered.fits
psf20_grn_60_vesta_od345_ama+42_recentered.fits
psf20_red_10_vesta_od160_ama+63_0p10.fits
psf20_red_10_vesta_od160_ama+63_0p10recentered.fits
psf20_red_10_vesta_od160_ama+63.fits
psf20_red_10_vesta_od160_ama+63_recentered.fits
psf20_red_20_vesta_od160_ama+63_0p10.fits
psf20_red_20_vesta_od160_ama+63_0p10recentered.fits
psf20_red_20_vesta_od160_ama+63.fits
psf20_red_20_vesta_od160_ama+63_recentered.fits
psf20_red_20_vesta_od345_ama-42_0p10.fits

psf20_red_20_vesta_od345_ama+42_0p10.fits
psf20_red_20_vesta_od345_ama-42_0p10recentered.fits
psf20_red_20_vesta_od345_ama+42_0p10recentered.fits
psf20_red_20_vesta_od345_ama-42.fits
psf20_red_20_vesta_od345_ama+42.fits
psf20_red_20_vesta_od345_ama-42_recentered.fits
psf20_red_20_vesta_od345_ama+42_recentered.fits
psf20_red_60_vesta_od160_ama+63_0p10.fits
psf20_red_60_vesta_od160_ama+63_0p10recentered.fits
psf20_red_60_vesta_od160_ama+63.fits
psf20_red_60_vesta_od160_ama+63_recentered.fits
psf20_red_60_vesta_od345_ama-42_0p10.fits
psf20_red_60_vesta_od345_ama+42_0p10.fits
psf20_red_60_vesta_od345_ama-42_0p10recentered.fits
psf20_red_60_vesta_od345_ama+42_0p10recentered.fits
psf20_red_60_vesta_od345_ama-42.fits
psf20_red_60_vesta_od345_ama+42.fits
psf20_red_60_vesta_od345_ama-42_recentered.fits
psf20_red_60_vesta_od345_ama+42_recentered.fits

10 Related documents

PACS Observer's Manual, HERSCHEL-HSC-DOC-0832, Version 2.3, 08-June-2011

Review on PACS bolometers time constant, Billot et al., SAp-FIRST-NB-0688-05 (expectations for PSF smearing by fast scan)

PACS Test Analysis Report FM-ILT - Part III PICC-ME-TR-007 Section 3.1.4 (D.Lutz) on Photometer Point Spread Function

Herschel/PACS modelled point-spread functions, N. Geis and D. Lutz, PICC-ME-TN-029 issue 2.0

In-orbit crosstalk in the PACS photometer, PICC-ME-TN-034, V1.1, September 25, 2009

Herschel stray light report, by the Herschel Straylight Working Group, SAp-HERSCHEL-KO-0723-10, V1.0, February 7, 2011

PACS spatial coordinates cheat-sheet, PICC-ME-TN-027, V 1.0, December 11, 2008

Non-linearity Correction Module for the PACS Photometer PICC-NHSC-TR-031, V0.2, February 2011

11 Appendix: Orientation conventions used in this note

The observations used for this note have been obtained with a variety of scanmap setups and with different orientations of the Herschel telescope on sky. During the reduction, all PSF maps have been created as if the spacecraft position angle PA would have been 0 at the time of observation, meaning the 'Z' direction is pointing up (=north) in the images[3]. The fits headers of the released PSF images are consequently manipulated to fiducial RA=DEC=POSANGLE=RA_NOM=DEC_NOM=CRVAL1=CRVAL2=CROTA2=0.

When referring to scan direction in comparison to the PACS array, we use the conventions of the PACS Observer's manual Section 5.1.1 (Figure 5.2). Given our images have been oriented with the Z direction up, the scan direction is best specified via the 'array-to-map angle' α, measured CCW from top in the PSF images. In some tables and in the PSF filenames, we abbreviate this array-to-map angle as 'ama'.

This 'array-to-map angle' α is identical to the HSPOT 'Orientation angle' (mapScanAngle in HCSS meta data) only if the HSPOT 'Orientation angle reference frame' (mapScanAngleRef in meta data) was set to 'Array' (HSPOT) which transfers to 'inst' (HCSS meta). It will differ if 'Sky' was used.

12 Document change record

Version	Date	Initials	Comment
0.1	2009-09-16	DL	Quick version
0.2	2009-10-27	DL	Added OD160 Vesta
0.3	2009-11-10	DL	Minor updates to Vesta PSF, bright source morphology
1.0	2010-10-22	DL	Major rewrite, based on HCSS 5.0 re-reduction
1.01	2010-11-03	DL	Added list with tarball contents
2.0	2012-04-04	DL	Major revision, HCSS 8.0 reduction and addition of new data
2.1	2015-06-08	DL	Added info and dedicated EEF for SPIRE/PACS parallel mode
2.2	2015-11-16	DL	Added dedicated EEF for 60arcsec/sec prime mode

[3]Note that at the time of writing V2.0 of this document, there were still issues with display orientation in HIPE, checking with e.g. DS9 is recommended in case of doubt.